FUTURE GENERATIONS OF LIGO MIRRORS

ANDREA MOSCHETTINI

Characterization of mechanical loss and optical absorption of amorphous and crystalline mirrors for application in gravitational wave detectors

MSc Engineering
Nanotechnologies for ICTs
Politecnico di Torino

Andrea Moschettini: *Future generations of LIGO mirrors,* Characterization of mechanical loss and optical absorption of amorphous and crystalline mirrors for application in gravitational wave detectors

SUPERVISORS:
Martin M. Fejer
Riccardo Bassiri
Ashot Markosyan
Enzo Mario Di Fabrizio

LOCATION:
Stanford University

TIME FRAME:
April 2023 - August 2023

ABSTRACT

This Master's thesis investigates the development of mirror coating materials with reduced thermal noise, aiming to advance the design of upcoming gravitational wave detectors. This work will develop as follows:

1. **LIGO Project**: This section provides an overview of gravitational waves and how they are detected. It introduces the *advanced LIGO* interferometer, detailing its operational principles, main features, and inherent limitations.
2. **Crystalline Coatings**: The first segment addresses the physical characterization of intrinsic defects in next-generation AlGaAs/-GaAs mirrors. This analysis employs photothermal common-path interferometry (PCI), a method innovated at Stanford University. The objective is to pinpoint issues that would make these industrial-grade mirrors non-compatible with LIGO's stringent requirements.
3. **Amorphous Coatings**: The subsequent segment delves into the design and fabrication of micro-resonators used to gauge the coating mechanical loss in amorphous oxide coatings at cryogenic temperatures, notably those involving Titania-doped Germania ($\mathtt{Ti}:\mathtt{GeO_2}$) layers alternated with Silica. This involves the use of Finite Element Modeling to simulate trident-shaped resonators that feature multiple high-Q resonant modes, the fabrication of these resonators in *cleanroom* environment, and *ring-down* measurements of mechanical loss— both for uncoated and coated samples. These measurements assist in assessing their mechanical loss (Q^{-1}), which is directly correlated to thermal noise.

The anticipated outcomes of this research project have the objective of qualifying and optimizing next generation mirror coating materials. The central emphasis lies in developing materials with minimized thermal noise, a trait crucial for improving the accuracy of gravitational wave detection.

https://ligo.stanford.edu/research

ACKNOWLEDGEMENTS

First and foremost, I would like to express my deepest gratitude to Professor Martin Fejer for providing me with the invaluable opportunity to be a part of the LIGO group at Stanford University. His guidance, mentorship, and unwavering faith in my capabilities have played a crucial role throughout the duration of my project.

I am especially indebted to my dedicated supervisors at Stanford, Riccardo Bassiri and Ashot Markosyan. Their meticulous feedback, constructive criticisms, and encouragement during the most challenging times have been instrumental in shaping the course of my research. Their relentless commitment and passion for discovery will serve as a beacon of inspiration for my future research pursuits. Our extensive discussions on history, life, culture, and countless other topics have enriched me and will be fondly remembered.

In conclusion, I want to express my gratitude to my PoliTO supervisor, Enzo Mario Di Fabrizio, and academic advisor, Carlo Ricciardi, for this precious opportunity.

CONTENTS

ACRONYMS

LIGO	Laser Interferometry for Gravitational-Wave Observatory
Q	Quality Factor
GW	Gravitational Waves
PCI	Photo-thermal Common-Path Interferometry
PD	Photo-Deflection
ppm	parts-per-million
ppb	parts-per-billion
AU	Arbitrary Units
SLD	Super Luminescent Diode
FEM	Finite Element Modeling
FS	Fused silica
XRD	X-Ray Diffraction
IBS	Ion Beam Sputtering
FWHM	Full-Width Half Maximum
AD	As Deposited
PCB	Printed Circuit Board

Part I

THE LIGO PROJECT

The Laser Interferometer Gravitational-Wave Observatory (LIGO) stands as a monumental effort in physics, conceived to directly detect gravitational waves. These waves, conceptualized as ripples in space-time, were a prediction of Einstein's general theory of relativity. LIGO's ambition transcends mere detection; it aspires to lead the nascent field of gravitational-wave astrophysics. With its advanced infrastructure, LIGO aims to shed light on the enigmatic recesses of the universe, revealing the mysteries of black holes, neutron stars, and other cosmic mysteries.

LIGO comprises two interferometers strategically positioned in Livingston, Louisiana, and Hanford, Washington. They employ laser light to measure distances between mirrors with remarkable precision. In 2015, when the initial LIGO detector was upgraded to the current state-of-the-art aLIGO (Advanced LIGO), the project achieved a historic feat by detecting gravitational waves from the merger of two black holes located over a billion light-years distant[30]. Since this groundbreaking observation, LIGO has cataloged a series of subsequent gravitational wave detections.

Beyond its primary duties, LIGO operates as a national nexus for gravitational-wave research, extending an invitation to the wider scientific community to collaborate on detector development, observational campaigns, and data analysis. Through its cutting-edge efforts, LIGO unveils a fresh lens to probe the cosmos and uncover its most profound secrets.

1

GRAVITATIONAL WAVES

Gravitational waves arise from non-uniformly distributed accelerating mass systems. These waves instigate dynamic strains in spacetime, modifying the lengths of objects in their trajectory. Due to the inherent weakness of gravitational interaction, only colossal masses under significant acceleration, such as during the merging of neutron stars, black hole binary systems, or supernovae explosions, have the potential to produce detectable gravitational waves.

The groundbreaking first detection of gravitational waves was made on September 14, 2015, by the Advanced LIGO (aLIGO) detector. The signal, labeled GW150914 [30], was traced to the spiraling and subsequent merging of a binary black hole system. This discovery was enabled by two 4-kilometer-long Michelson-based interferometers situated in Hanford, Washington State, and Livingston, Louisiana, USA.

1.1 GRAVITATIONAL RADIATION

Within the context of Einstein's general relativity, gravitational waves are conceived as transverse waves that travel at light speed and radiate from accelerating masses. While bearing similarities with electromagnetic waves, a crucial distinction exists. Electromagnetic waves are inherently dipolar, given the equilibrium between positive and negative charges. However, the conservation of mass governs momentum, ensuring that the center of mass (the dipole moment of a mass distribution) remains unaccelerated in isolated systems. Consequently, the lowest order radiating term is predominantly quadrupolar, emanating solely from the acceleration of asymmetrical mass distributions.

Transverse waves vibrate perpendicular to their propagation direction.

Figure 1 showcases a representative theoretical experiment detailing the impact of a transiting gravitational wave on a collection of test masses. This wave periodically distorts the surrounding space, as seen in (a) and (b). A gravitational wave advancing along the z-axis elongates the ring along the y-axis, simultaneously squeezing it along the x-axis. During the subsequent half-cycle, the effect is reversed. The condition in (a) is termed the *plus polarization state*, while (b) —which causes an analogous distortion, but with axes rotated by 45 degrees— is termed the *cross polarization state*. The resulting deformation is measurable by observing the displacements of the test masses due to the incoming wave. For a particle ring with radius L that elongates by an amount ΔL in one direction and compresses by

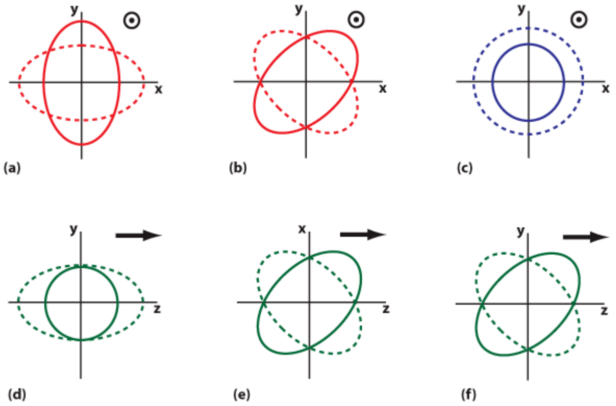

Figure 1: Illustration of the effects of six potential polarizations of gravitational waves on a ring of freely-falling test masses. Only (a) and (b) are predicted by General Relativity. [13]

the same measure orthogonally, the gravitational wave strain is represented as

$$h = \frac{2\Delta L}{L} \tag{1}$$

This strain characterizes the fundamental mechanism of gravitational wave detectors. Remarkably, even for events on a cosmic scale, a strain value of just $h \approx 10^{-21}$ is typically anticipated.

1.2 GRAVITATIONAL WAVE SOURCES

While any object with mass that accelerates can, in principle, emit gravitational waves, terrestrial objects' masses and accelerations are insufficient for the generation of gravitational waves detectable by current instrumentation. Therefore, one should focus on the vast expanse beyond the Solar System. Each class of celestial entities produces a distinct or characteristic set of signals that LIGO's interferometers are tuned to detect and analyze through the LIGO data infrastructure.

COMPACT BINARY INSPIRAL GRAVITATIONAL WAVES

Compact Binary Inspiral gravitational waves constitute the main class of gravitational waves that LIGO is engineered to identify. To date, they remain the sole gravitational wave type that was empirically confirmed. These waves originate from dense object pairs like white dwarf stars, black holes, or neutron stars. As these objects orbit each other, they radiate gravitational energy, with each pair generating a unique gravitational wave pattern. However, a common theme among these patterns is the *inspiral* mechanism.

This inspiral phenomenon evolves across millions of years. Pairs of compact, dense objects in mutual orbit radiate gravitational waves, leading to energy dissipation from their orbital system. Over time, this causes the objects to spiral closer together. Their orbits accelerate due to the decreased distance, resulting in even more intense gravitational wave emissions. The consequent energy loss from the system further enhances their proximity. This positive feedback persists, propelling the objects into an accelerating spiral that culminates in their eventual merger.

LIGO's instrumentation can pick up specific gravitational wave frequencies aligned with many of the phenomena described above. As these orbiting entities inch closer and orbit faster, they emit gravitational waves within LIGO's detection bandwidth. However, the duration for which they resonate within this detectable frequency band is relatively fleeting.

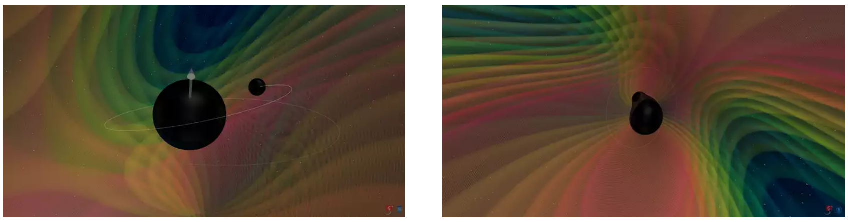

(a) Inspiral orbitation of two black holes

(b) Black holes converging into a merger

Figure 2: Numerical simulation of a black-hole binary merger with asymmetric masses and orbital precession (signal GW190412). Figures developed by N. Fischer, H. Pfeiffer, A. Buonanno (Max Planck Institute for Gravitational Physics), as part of the Simulating eXtreme Spacetimes project.

CONTINUOUS GRAVITATIONAL WAVES Continuous gravitational waves are believed to emanate from singular, massive rotating objects, such as neutron stars. A neutron star with any deformities or anomalies in its otherwise spherical shape would produce gravitational waves. If its rotation rate remains stable, this star will consistently emit gravitational waves with a steady frequency and amplitude.

STOCHASTIC GRAVITATIONAL WAVES Though there may not be many dominant sources of either continuous or binary inspiral gravitational waves, this doesn't imply a quiescent universe from LIGO's perspective. Many smaller gravitational waves, emanating from various directions, culminate to form what is termed a *Stochastic Signal*. The origins of these waves are manifold: they could be remnants from the Big Bang, or byproducts of phenomena like BBH (Binary Black-Hole), BNS (Binary Neutron Star), supernovae, kilonovae, or asymmetrically rotating neutron stars. All these sources confluence

'Stochastic' alludes to the inherent unpredictability of a pattern, amenable to statistical analysis.

to form a stochastic background that stands as a testament to the cosmos's dynamism.

BURST GRAVITATIONAL WAVES Distinct from the patterns or continuous waves seen elsewhere, burst gravitational waves emerge from short-lived events, their signatures being erratic and unpredictable, such as supernovae. Their fleeting nature and relatively low mass compared to compact binary renders them difficult to analyze, as they need to happen within a short distance (e.g., within the Milkyway) to be succesfully detected.

1.3 EXAMPLE OF GRAVITATIONAL WAVE OBSERVATION

On August 17th, 2017, at 12:41:04 UTC, aLIGO detected a signal lasting nearly 100 seconds, in which the frequency increased continuously. It was first detected by the LIGO Livingston detector, and, after a three-millisecond interval, reached the LIGO Hanford detector. Notably, this signal traversed through the most sensitive frequency range of these detectors, spanning from 10 Hz to 100 Hz. A visual representation of the signal's amplitude changes in the final 30 seconds of the event can be seen in Figure 3. By evaluating the observed duration of the inspiral and its ultimate frequency, it was deduced that the signal's origin could be attributed to the merging of a low-mass two-body system, specifically identified as a binary neutron star.

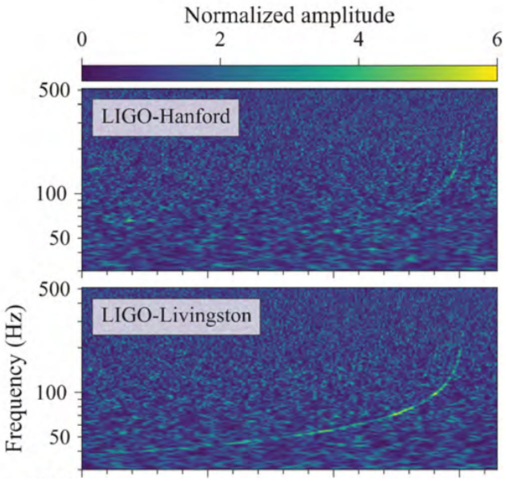

Figure 3: Time-Frequency representations of the gravitational-wave event GW170817 as observed by the LIGO Hanford (top) and LIGO Livingston (bottom) detectors. Times are referenced to August 17, 2017, 12:41:04 UTC. [31]

2

LIGO INTERFEROMETER: AN EXAMINATION

When a gravitational wave traverses the aLIGO detectors, the phenomenon manifests as a periodic alteration in the arm lengths of the interferometer's arms — one elongating while the other contracts, and then the pattern reverses —. This phenomenon is termed *differential arm motion* or differential displacement due to its simultaneous and contrary effects on arm lengths. Despite the apparent simplicity of this principle, the detection of such changes induced by gravitational waves presents a formidable challenge. The size of these perturbations may be as minute as one ten-thousandth the diameter of a proton (i.e., 10^{-19} m).

2.1 ENHANCING A MICHELSON INTERFEROMETER

A Michelson interferometer (refer to Figure 4) is an optical apparatus that dissects a light beam into two independent beams. These beams then navigate along perpendicular trajectories before reuniting, thereby creating an interference pattern.

The fundamental configuration includes a light source (commonly a laser), a beam splitter, a pair of mirrors (test masses), and a detector. The beam splitter divides the incoming light beam into two equivalent fractions, which subsequently reflect off the pair of mirrors positioned perpendicularly to each other. The reflected beams then travel back to the beam splitter where they merge and interfere.

The resultant interference pattern, which manifests as an array of luminous and dark fringes, is registered by a photodetector. Modifying the path length of one of the beams — achievable through mirror displacement or the introduction of a sample into the beam — can alter the fringe positions.

Modern interferometric gravitational wave detectors utilize extended baselines or arm lengths to enhance detection sensitivity. However, practical constraints, including cost especially, and the Earth's curvature, limit the feasible arm lengths for these typically ground-based detectors. In order to maximize gravitational wave sensitivities, several advanced technologies have been designed and incorporated, thereby serving as enhancements to the basic Michelson interferometer design [5].

- **Fabry-Perot cavities**: Positioned close to the beam-splitter, the inner mirrors exhibit partial transmittance, while the end mirrors are highly reflective. Light is effectively stored within the cavities (maintained at resonance) while oscillating between the

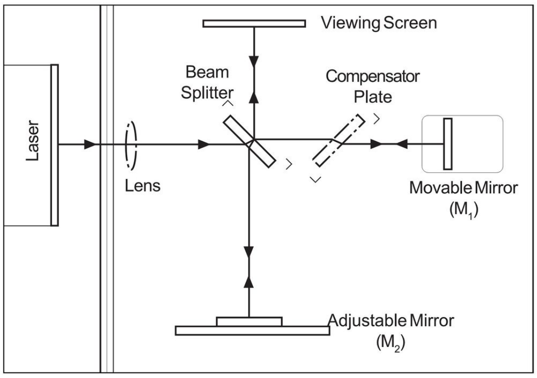

Figure 4: Basic schematics of a Michelson interferometer. A compensation plate is incorporated to counterbalance any undesired phase shift introduced between the two beams by the beam splitter. [17]

inner and outer mirrors several times before eventually leaking out and reaching the detector.

- **Power and signal recycling**: The insertion of extra mirrors into the laser path can effectively amplify the amount of light reaching the detector, thereby enhancing the system's overall sensitivity. A power recycling mirror is positioned along the laser input path to create a cavity with the interferometer itself. In contrast, a partially transmitting signal recycling mirror is placed between the beam splitter and the photodetector to recycle light back into the detector and boost sensitivity at specific frequencies of interest.
- **Squeezed light**: Classical coherent electromagnetic waves have well-defined amplitude and phase. However, in quantized coherent fields, amplitude and phase harbor inherent uncertainties, independent of each other. Manipulating the light field to reduce amplitude uncertainty inadvertently enhances phase fluctuations. Nevertheless, by suitable manipulation, it is possible to minimize uncertainties in the amplitude or phase of the quantized field below the level of uncertainty inherent in vacuum fluctuations.

A-LIGO CONFIGURATION The experimental setup employs Michelson's design principle, using a single laser operating at a wavelength of 1064 nm up to 125W (currently fixed at 60W)[1]. The laser serves as the primary means to detect any positional shifts in the end test mass optics (ETMs). By measuring the differential change in arm length, this variation is continuously monitored over time at the detector's output.

LIGO Hanford and LIGO Livingston are designed to be as similar as possible to minimize discrepancies between detectors, thereby facilitating cooperative noise reduction efforts. The aLIGO detectors

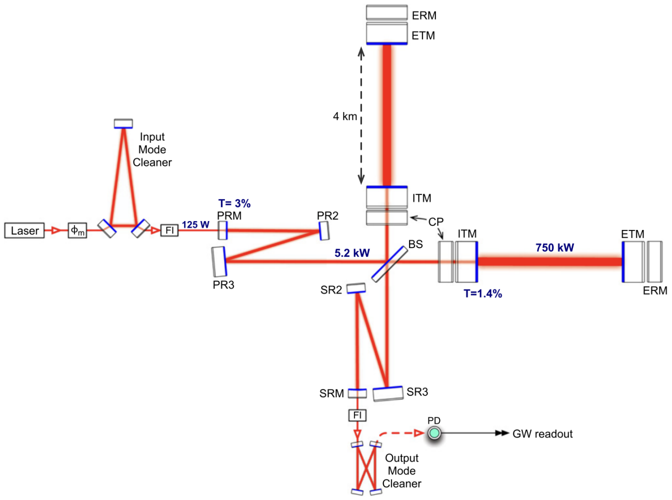

Figure 5: Schematics of an Advanced LIGO detector, highlighting the additional components that augment its operation compared to a standard Michelson interferometer: Fabry-Pérot cavities in grey, input mode cleaning in green, and output mode cleaning optics in blue. [1]

incorporate two Fabry-Pérot cavities, each extending 4 km in length. Currently, each cavity yields a combined circulating cavity power of 375kW. The test mass mirrors, weighing 40 kg and with a diameter of 34 cm, are fabricated from high-quality Fused Silica (FS). To amplify reflectivity and mitigate the impact of laser heating, these test masses are coated with highly reflective dielectric mirrors with low optical absorption.

As depicted in Figure 5, the laser light enters the detector and crosses the input mode cleaner (IMC) optics. These optics serve dual purposes. They suppress the intensity of stray polarized laser light and filter the optical modes of the laser light, permitting only the Gaussian TM00 mode to pass through.

Subsequently, the laser light encounters a beam splitter mirror, which segregates it into two separate arms, each housing a Fabry-Pérot cavity. Within these cavities, the laser light reflects continually between the partially transmissive input test mass (ITM) mirrors and the end-test masses (ETM). This configuration facilitates an *on resonance* state for the optical cavity, allowing significant laser power accumulation during each 8 km round trip.

A small fraction of the laser light transmits through each ITM, and the two beams reunite at the beam splitter. Following this, the combined beams traverse a final set of output mode cleaner filters, eliminating any higher-order optical modes, thereby significantly reducing the power that requires detection at the output.

2.2 SOURCES OF NOISE IN LIGO DETECTORS

Noise from various sources significantly impacts the detectors' ability to measure Gravitational Waves. Figure 6 illustrates the collective impact of these noise sources on the sensitivity of the detector.

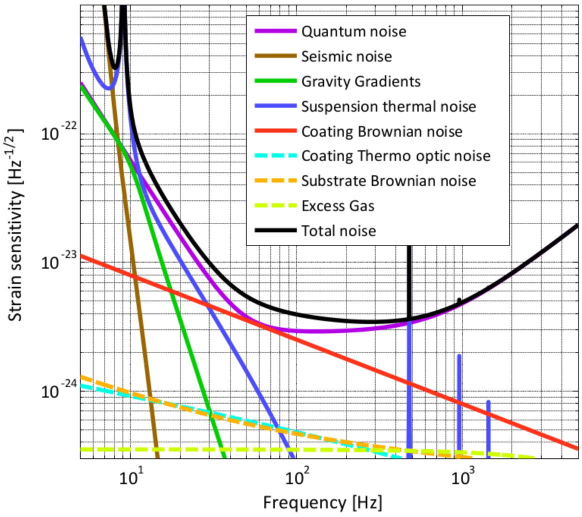

Figure 6: Power spectral density of noise sources forming the noise budget for Advanced LIGO. [18]

QUANTUM NOISE The Standard Quantum Limit (SQL) serves as a theoretical threshold for detector sensitivity, dictated by the balance between two major components:

- **Photon shot noise**, an intrinsic noise source, arises from the statistical accounting of photons striking the photodetector at the output of the interferometer. This issue imposes a limit on detector sensitivity that is proportional to the square root of the photon count, as per Poisson's distribution. The effect on strain sensitivity depends on the frequency of the gravitational wave (f), which is defined by the following equation [14]:

$$h_{shot}(f) = \frac{1}{L}\left(\frac{\hbar\lambda\pi}{2P\epsilon c}\right)^{\frac{1}{2}} \frac{f}{\sin(\pi f\tau)}, \tag{2}$$

  where:

L is the length of the interferometer arm,
$\hbar$ the reduced Planck's constant,
P the power of the incident laser,
λ the wavelength of the incident laser,
c the speed of light in a vacuum,
ϵ the quantum efficiency of the photodiode detector, and
τ the storage time within the detector.

One effective strategy to minimize photon shot noise, as inferred from the equation, is to increase the laser power and adjust the storage time to half the wave period. These adjustments can be accomplished via power and signal recycling components.

- **Radiation pressure noise** is a function of laser power and is triggered by the momentum transferred from incoming photons to the suspended test masses. This variation in strain is quantified by the following equation [20]:

$$h_{rp} = \frac{N}{mf^2L}\sqrt{\frac{2\hbar P}{\pi^3\lambda c}}, \tag{3}$$

  Here, N represents the number of cycles of the laser beam traversing the $2L$ long path in the interferometer arm, and the remaining symbols carry the same definitions as in equation 2.

Raising the laser input power reduces shot noise but simultaneously amplifies radiation pressure noise. Therefore, the SQL is determined by the condition at which $h_{shot} = h_{rp}$, a state that cannot be surpassed with current technology. It should be noted, however, that the noise levels in contemporary detectors still remain above the SQL.

SEISMIC NOISE Seismic noise, emanating from terrestrial surroundings, represents an additional noise source. This noise category encompasses diverse forms, from earthquakes to human activities such as road traffic, and often exhibits erratic behavior. Thus, it is critical to minimize the influence of these noise sources on the detector test masses. This is achieved using techniques such as spring stacks for vertical isolation and multi-stage pendulums for horizontal isolation, as depicted in Figure 7 [28]. When the frequencies exceed the resonant frequency of each pendulum, the transfer function decreases proportionally to $\frac{1}{f^2}$, effectively isolating the mirror from its suspension point's movement.

In Advanced LIGO, the lowest level of isolation is achieved by the Hydraulic External Pre Isolator (HEPI) stages [16]. These stages consist of four corner stations on each vacuum tank securely attached to the ground, allowing them to move in unison with it. Utilizing hydraulic actuators, they compensate for ground acceleration in all six degrees of freedom, thereby providing low-frequency isolation ranging from 0.1 Hz to 10 Hz. The movement of the second stage is linked to the first stage using a feed-forward loop to detect the motion of HEPI and minimize the motion of the second stage to nearly zero.

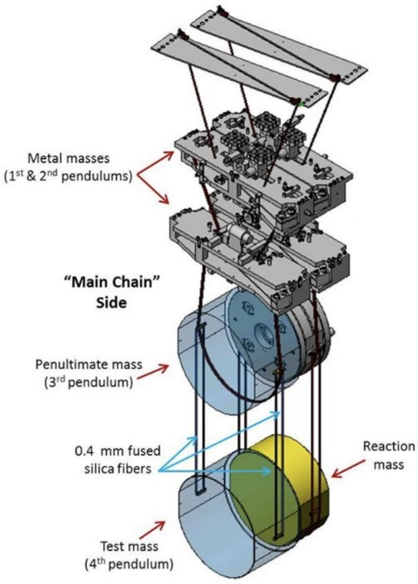

Figure 7: The test masses of Advanced LIGO are suspended at the lower end of a pendulum consisting of four segments. LIGO utilizes the fundamental concepts of pendulum dynamics, where each segment within the pendulum absorbs motion from the segment above it, isolating the motion from propagating to the segment below.

GRAVITY GRADIENT NOISE Gravity gradient noise arises from fluctuations in the local gravitational field around a detector, which directly affect the detector mirrors' position through gravitational forces. This noise presents a significant obstacle in the detection of gravitational waves, particularly in the 6 to 20 Hz frequency range. The main source of this noise is seismic waves propagating across the Earth's surface. These waves induce density fluctuations in the Earth near the detector, resulting in fluctuating gravitational forces acting on the test mass.

The effects of surface waves can be mitigated by installing multiple seismometers at different locations around the detector to measure these waves' impact. This data can then be used to actively counteract or remove some of their effects from the interferometer [25]. Furthermore, constructing future detectors at depths of 100 to 200 meters underground can significantly decrease the influence of surface seismic waves. This reduction is because the energy of a surface wave exponentially diminishes as it travels through increasing amounts of material.

THERMAL NOISE Thermal noise serves as a significant constraint on detector sensitivity within the frequency range of interest for LIGO operation (several tens to a few hundred Hz). This noise originates from the Brownian motion of atoms and molecules in the materials used in interferometers, particularly in the test masses, mirror coatings, and suspensions. There are two types of thermal noise in detector optics: one stems from internal friction due to localized mechanical loss sources, such as material structure defects, and the other from statistical temperature fluctuations.

Mechanical-loss-induced thermal noise, also known as *Brownian noise*, can be characterized in terms of the thermal energy associated with each resonant mode of the material. According to the equipartition theorem, this amounts to $\frac{1}{2}k_B T$ per degree of freedom. On the other hand, statistical temperature fluctuations in a material can interact with properties like local expansion and changes in refractive index, collectively producing a noise source referred to as *thermo-optic* noise. The primary objective of this study is to perform a comprehensive characterization of novel coatings applied to the mirror test masses. The aim is to mitigate the detrimental effects of mechanical loss and optical absorption in order to minimize thermal noise in particular, ultimately enhancing the sensitivity of the detector. For this reason, further details about this matter will be discussed in the following section.

2.3 MECHANICAL LOSS IN COATING MATERIALS - THERMAL NOISE

Since coating thermal noise is currently the most significant limitation on the detectors' sensitivity, a thorough understanding of it is necessary, so that its impact can be accurately quantified and its causes identified. Dielectric mirror coatings used in gravitational wave detectors consist of alternating layers of materials with different refractive indices, achieving high reflectivity.

2.3.1 *Fluctuation-dissipation theorem*

The atoms and molecules in the test masses and suspensions undergo unpredictable Brownian motion due to their finite temperature. This motion manifests as thermally induced vibrations in the system's resonant modes. The fluctuation-dissipation theorem [7] explains the relationship between this thermal motion and the mechanical loss (or internal friction) of the materials comprising the test masses. The theorem can be expressed as:

$$S_x(\omega) = \frac{4k_B T}{\omega^2}\Re\left[\frac{1}{Z(\omega)}\right]. \tag{4}$$

Equation 4 correlates the power spectral density of the thermal displacement, $S_x(\omega)$, with the real part of the mechanical impedance, $Z(\omega)$. The mechanical impedance indicates the material's delay in strain response to an external force. It's possible to model the vibrational modes as lightly damped harmonic oscillators, which allows the mechanical impedance to be expressed in terms of the mode's resonant frequency and a loss factor, $\phi(\omega)$, which represents the system's phase delay. Specifically, it can be written as:

$$\Re\left[\frac{1}{Z(\omega)}\right] = \frac{\omega_0^2\phi(\omega)}{m(\omega_0^4\phi^2(\omega) + (\omega_0^2 - \omega^2)^2)}; \tag{5}$$

Consequently, operating sufficiently far from the system's resonant frequencies, a low-loss material will naturally guarantee lower mechanical dissipation and thus lower thermal noise.

The thermal noise can be calculated from the power dissipated in the test-mass mirror, assuming an application of pressure identical to the spatial profile of the laser beam on the test-mass mirror's front face. The fluctuation-dissipation theorem can then be used to compute the power spectral density, $S_x(f)$, of the thermal displacement as follows:

$$S_x(f) = \frac{2k_B T}{\pi^2 f^2}\frac{W_{diss}}{F_0^2}, \tag{6}$$

where F_0 is the peak amplitude of the external oscillatory force and W_{diss} is the power dissipated in the mirror, which can be written as:

$$W_{diss} = 2\pi f U_{max}\phi(f). \tag{7}$$

Here, U_{max} is the total energy associated with the peak elastic deformation of the test mass.

Moreover, the different thermo-mechanical properties of the materials used for the substrate and in the multilayer coatings lead to another noise source known as thermoelastic noise. Small temperature variations cause displacements in the front mirror surfaces due to the coating material's thermal expansion, characterized by the thermal expansion coefficient, α. The spectral density of thermoelastic thermal noise arising from a dielectric coating of thickness d was carried out by professor Fejer [12] and reported in Equation 8 (the subscript s represents a property of the substrate).

$$S_x(f) \approx \frac{8k_B T^2}{\pi\sqrt{2\pi f}}\frac{d^2}{\omega^2}(1+\sigma_s)^2\frac{C_{avg}^2}{C_s^2}\frac{\alpha_s^2}{\sqrt{\kappa_s C_s}}\tilde{\Delta}^2, \tag{8}$$

where

$$\tilde{\Delta}^2 = \left\{\frac{C_s}{2\alpha_s C_{avg}}\left[\frac{\alpha}{1-\sigma}\left(\frac{1+\sigma}{1+\sigma_s} + (1-2\sigma_s)\frac{Y}{Y_s}\right)\right]_{avg} - 1\right\}^2. \tag{9}$$

In the latter two equations,

C	is the specific heat capacity
κ	is the thermal conductivity
σ	is the Poisson's ratio
Y	is the Young modulus

2.3.2 *Amorphous and crystalline materials*

Amorphous materials are distinguished by an absence of long-range order at the atomic or molecular level. This disordered arrangement leads to the manifestation of Two-Level Systems (TLS) [15], which conceptualize energy coupling from the elastic field into low energy excitations present in the amorphous material. In the context of TLS, specific regions within the material contain atoms or small groups of atoms that have two energetically similar configurations they can exist in. These configurations can be visualized as two nearly identical energy wells. With even a slight perturbation, such as thermal fluctuations or an external force, these atoms or groups can transition between these configurations. The propensity for these transitions, activated by Brownian motion, contributes significantly to the mechanical loss of amorphous materials. Moreover, due to the close proximity of energy states, the energy landscape of amorphous materials is rather dense, making transitions between these states relatively frequent. The particular distribution of these energy wells gives rise to temperature-dependent peaks in the mechanical loss. Data for losses over temperature ranges including cryogenic thus serve as a useful *spectroscopic* tool for TLS distributions, serving to refine theoretical models.

Crystalline materials are characterized by a highly ordered, repeating atomic or molecular structure. This order extends over longer distances, giving rise to a clear, well-defined energy landscape. In this landscape, potential configurations for atomic or molecular positions are separated by more substantial energy barriers. As a consequence, transitions between these states are less frequent and often necessitate a more considerable amount of energy. One challenge intrinsic to crystalline structures, especially in optical applications, is birefringent noise. Birefringence, in essence, refers to the differential refraction of light based on its polarization and direction as it passes through a material. In crystalline materials, inherent strains or imperfections can cause fluctuations in this birefringence, termed birefringent noise. These fluctuations in the refractive index can lead to phase noise, which can interfere with the accuracy and precision of optical measurements or applications. It's worth noting that this phenomenon is specifically associated with the ordered nature of crystalline materials and is not observed in amorphous counterparts.

In summary, due to their inherent properties, crystalline coating materials are anticipated to be the future for LIGO mirror applications, with potential reductions in overall thermal noise. Nonetheless, the development of an optimal deposition process is essential to ensure maximum uniformity and minimal internal stress. Moreover, the scale required for LIGO test masses presents an economic challenge.

Part II

OPTICAL ABSORPTION IN ALUMINUM GALLIUM ARSENIDE MIRRORS

Mechanical dissipation in high-reflectivity optical coatings, a phenomenon worsened by coating Brownian noise, is a considerable impediment for advanced precision measurement apparatus, including gravitational wave detectors. Recent progress in the realm of cavity quantum optomechanics heralds an innovative resolution to this intricate problem. This scientific discipline capitalizes on optomechanical interactions within optical cavities [8] to manage and investigate the quantum characteristics of mechanical oscillators over an array of scales, from nanometers to the macroscale. Attaining the quantum regime of mechanical motion necessitates structures exhibiting outstanding optical and mechanical quality.

In this context, monocrystalline $GaAs/Al_xGa_{1-x}As$ heterostructures, specifically AlGaAs, have been identified as potential candidates for multilayer mirror applications [19]. The present section is dedicated to scrutinizing the intrinsic defects of the mirror coatings via the measurement of their optical absorption, employing two techniques: Photothermal Common-Path Interferometry (PCI) and Photodeflection (PD).

3

INVESTIGATION METHODOLOGY

3.1 METHOD: PHOTOTHERMAL COMMON-PATH INTERFEROMETRY (PCI)

Photothermal common-path interferometry (PCI) represents a cutting-edge approach explicitly designed for characterizing materials with low optical absorption. This technique deploys two distinct lasers identified as the *pump* and the *probe*. The underlying methodology involves employing a low-power probe beam to discern the thermal effect incited by the sample's absorption of the higher-power pump beam. The pump beam, characterized by higher power and a reduced waist with respect to the probe, undergoes modulation to generate AC thermal effects on the sample at a frequency determined by the chopper. The resultant heat, produced by the absorbed pump, disrupts the Gaussian profile of the probe beam at its nucleus, thus inducing interference between the deformed and the unaffected segments of the probe beam.

The perturbation of the probe beam initially manifests as a minor disruption of the wavefront, primarily guided by temperature-dependent refractive index alterations ($\frac{dn}{dT}$). However, other subtle effects, such as thermal expansion and photoelastic refractive index changes due to localized stresses within the heated region's proximity, may also contribute. To elaborate on the phenomenon:

1. An interaction between the pump beam and the material initiates a phase disturbance, triggered by aspects like temperature-induced refractive index modifications, thermal expansion, and localized stresses.

2. As the probe beam traverses the material, the phase disturbance accumulates, altering the interference pattern, a result of the superposition of the perturbed and unperturbed sections of the probe beam.

3. The emerging interference pattern is delineated by regions of constructive and destructive interference, dictating the intensity or brightness distribution within the resulting beam profile.

4. The variations in intensity instigated by interference facilitate amplitude contrast, characterized by the intensity differential between areas of constructive interference (illuminated regions) and those of destructive interference (shadowed regions).

EXPERIMENT SETUP The interference pattern attains its maximum, dependent on multiple parameters, including the absorption coefficient. This maximum interference point is captured at a proximity as close as feasible to the Rayleigh range of the thermal lens and is detected by a photodetector and subsequently processed through a lock-in amplifier.

The Rayleigh range of a laser beam is the distance from the beam waist where the mode radius increased by a factor square root of 2.

Notably, the single-beam interference signal generation in PCI enables the achievement of a substantial amplitude contrast on the probe, thanks to the technique's near-field detection. This implies that despite the involvement of a single beam, the resultant interference effect can exhibit a magnitude comparable to that witnessed in traditional two-beam interferometers.

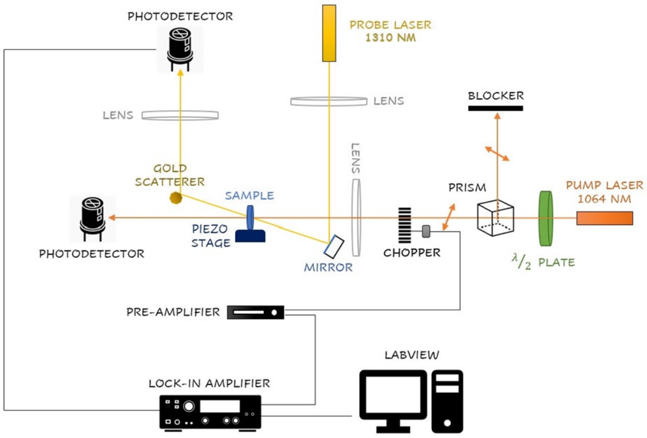

Figure 8: Simplified schematics of the PCI setup used for AlGaAs optical absorption measurements. The laser beams are aligned to make a 9° angle between them. An iris is mounted in the photodetector that captures the probe beam to isolate only the central peak of the interference pattern. This operation is simplified by the gold scatterer, which widens the beam, and hence the self-interference pattern. A half-wavelength plate rotates the polarization vector so that a prism can transmit only a part of the power, according to Malus's law. The power is monitored using the photodetector that captures the pump beam, available after moving away the sample by means of a motorized stage.

Pump laser is used at maximum power to minimize FWHM of the Gaussian profile, hence the additional components are needed to tune the power.

The initial task is to superimpose the pump beam onto the same xz-plane as the probe beam, an operation fundamental to the establishment of the PCI regime. Subsequently, the point of intersection must be shifted towards the sample. It should be noted that an alteration in the pump beam's position along the x-axis simultaneously modifies the crossing point's position within the z-direction. Consequently, both degrees of freedom must be judiciously manipulated concurrently to ensure that the point of intersection resides within the focal plane of the probe beam.

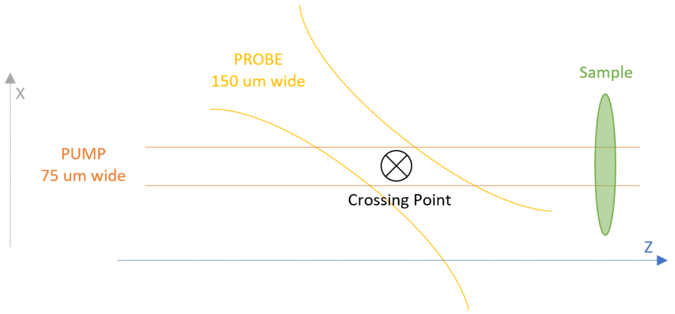

Figure 9: The alignment of pump and probe beams necessitates precise adjustments of their relative positions. The pump's position can be manipulated via a pair of mirrors, while the sample's position can be adjusted using the motorized stage, ensuring that the central maxima of both pump and probe intersect within the sample's focal plane.

The beam waists of the pump and probe are predetermined by the laser technology and the experimental configuration. However, it should be noted that under these circumstances, the Gaussian shape of the probe tends to integrate over multiple fringes of the thermally induced wave generated by the modulated pump on the sample's surface. This can potentially introduce complications with the absolute calibration for point-absorbing defects. One potential mitigation strategy for this issue could be to decrease the frequency of the chopper, considering the thermal diffusion length is inversely proportional to the square root of the frequency. Nevertheless, this adjustment would inadvertently augment the electrical noise due to the fact that the employed low-pass filter has a cut-off frequency of 10 Hz. Furthermore, the thermal influence of a point absorber on the substrate could be analogous to that of the pump beam itself, especially if the thermal diffusion length of the thermally induced wave is large relative to the size of the defect. Nonetheless, a discrepancy in the absorption value should still be perceptible.

CALIBRATION PROCESS PCI demonstrates high capability for relative measurements, rendering it ideal for juxtaposing results for homogeneous object types. This is due to the linearity of the photothermal signal and the inherently indirect detection of the absorbed pump power, facilitated by the probe beam. Subsequent discussions on AlGaAs defects will leverage this advantageous feature of PCI.

Nonetheless, it is critical to acknowledge that different materials induce distinct responses to pump absorption due to their unique physical properties. Therefore, the undertaking of absolute absorption loss measurements, necessary for qualifying materials for LIGO mirrors, requires calibration relative to appropriate reference samples. These reference samples should be similar objects possessing known absorption values. Practical selections in this context are neutral density filters, specific for both bulk and surface absorption measurements. Responses of these filters are illustrated in Figure 10, under the following process parameters: a pump power of 20 mW, pump wavelength of 532 nm, chopping frequency of 380 Hz, a probe-pump crossing angle of 0.12 rad, surface filter absorption of 22.2%, and bulk filter absorption of 44.9%/cm [2].

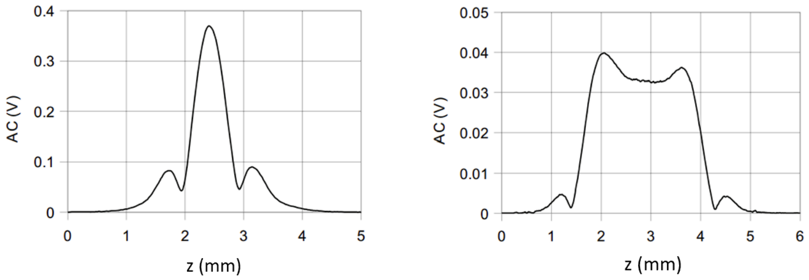

(a) Z-scan of ND surface filter.

(b) Z-scan of ND bulk filter.

Figure 10

The surface filter implemented in our apparatus comprises a fused silica substrate overlaid by a thin platinum layer, while the bulk filter consists of Schott glass #12. Given optimal setup alignment, the surface scan portrays a central maximum corresponding to the location where the pump and probe intersect at the sample surface. The width of this peak correlates with the system's depth space resolution. Similarly, the bulk absorber displays distinct features associated with the front and back surfaces of the sample, appearing as interference fringes. The values derived from the central peak of the surface absorber and the mid-plane of the bulk absorber serve calibration purposes, enabling the computation of absolute absorption through the ensuing formulas.

$$\mathrm{SURF}: \alpha_x = \mathrm{Corr} \cdot \left(\frac{V_{AC}/V_{DC}}{W_P}\right)_x \cdot \left(\frac{W_P}{V_{AC}/V_{DC}}\right)_{ST} \cdot \alpha_{ST} \quad (10)$$

$$\mathrm{BULK}: \alpha_x = \mathrm{Corr} \cdot \left(\frac{V_{AC}/V_{DC}}{W_P(1-R)}\right)_x \cdot \left(\frac{W_P\sqrt{T}}{V_{AC}/V_{DC}}\right)_{ST} \cdot \alpha_{ST} \quad (11)$$

where:

Corr	is the material-specific correction factor
V_{AC}/V_{DC}	signifies the modulation depth
W_P	represents the pump power
α	is the absolute absorption value
x	stands for the sample material
ST	symbolizes the reference material

For materials diverging from the absorption reference, a single value designated as the *correction factor* can be employed to compute absolute absorption. Factors such as thermal conductivity and $\frac{dn}{dT}$, along with other material properties, substantially influence this component. Anisotropic materials additionally introduce an orientation dependent constituent to this value. Experimental setup-intrinsic variables, like the pump waist radius and chopping frequency, exhibit a minimal impact, thereby supporting the use of a consistent material correction factor across varied PCI designs, given the relatively weak dependency on these variables.

Correction factors for a wide array of optical materials have been determined thus far through empirical or theoretical calculations. Fused silica is commonly found among optical materials, and it is often used as a reference due to its exceptionally low absorption, optical microscopy-favorable transparency, and a thermal response primarily influenced by $\frac{dn}{dT}$. The modulation depth is defined by the ratio of the AC thermal response to the chopped pump absorption, representing the PCI signal, to the total DC transmitted probe signal. This normalization procedure is essential for the accurate comparison of PCI signals derived from diverse samples.

The integration of a three-dimensional crossed pump/probe setup facilitates the simultaneous detection of absorption losses within both the tested material's bulk and its surface (coating), achievable via a single longitudinal depth scan, as depicted in Figure 11.

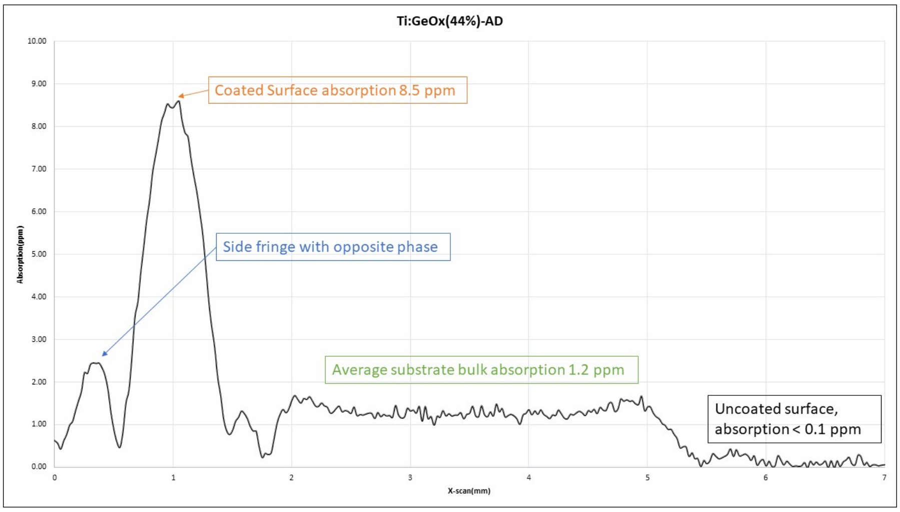

Figure 11: Longitudinal scan of fused silica substrate coated with $\mathrm{Ti} : \mathrm{GeO}_2$ layer.

The comprehensive photothermal response is a vectorial summation of signals deriving from diverse sources. Specifically in the context of our experiments, these sources include the substrate and its coating. These vectorial signals inherently possess two defining attributes: amplitude and phase. Moreover, it is noteworthy that the magnitude of the surface maximum exhibits a dependence on the bulk absorption. The peak associated with the surface is found to be located at the midpoint of the slope, indicative of the increasing signal attributable to bulk absorption. This stems from the configuration at the point of pump-probe alignment, where only half of the overlapping area is embedded within the substrate, while the remaining area lies outside.

To precisely distinguish between a thermally induced effect and a distinct kind of modulation, calibrating the phase delay between the chopper frequency and the PCI AC response is imperative. A thorough exploration of this subject, particularly focusing on defects within the AlGaAs layer, will be presented in Chapter 4. This phenomenon primarily concerns the time delay of the pump-absorption-induced lensing effect on the probe wavefront due to thermal diffusion, culminating in the aforementioned phase delay and interference pattern.

This calibration procedure is straightforwardly implemented by determining the phase delay between the probe signal and its own oscillation in the absence of pump-sample interaction. The observed phase delay is subsequently nullified using the lock-in amplifier. Then, the phase delay measured between the pump signal and the thermally-modulated probe interference peak is normally around 60^{circ}.

3.2 PHOTODEFLECTION TECHNIQUE

The photo-deflection (PD) technique, analogous to PCI, also exploits a pump-probe arrangement to leverage the photo-thermal effect. This principle of PD is aptly designed to measure residual absorption in both bulk materials and thin films. When the pump laser irradiation is absorbed, it creates a temperature differential between the irradiated and non-irradiated regions of the material. This temperature gradient subsequently induces a refractive index gradient - also known as a *thermal lens* - as a result of the thermally induced stress. Consequently, a probe beam traversing perpendicularly through the sample (subjected to a Gaussian pump laser beam of intensity $\frac{2P}{\pi w_p^2}$) is deflected by an angle denoted by:

$$\Theta = \frac{1}{n}\frac{dn}{dT}\frac{1}{\kappa}\frac{P}{\pi w_p}\epsilon_u \tag{12}$$

where:

κ	represents the material's thermal diffusion constant
P	is the pump power
w_p	is the pump beam waist
ϵ_u	is the absorption in a uniform region

The experimental configuration utilized is that in Figure 9, but with some minor tweaks. However, a mirror is purposefully positioned behind the sample, redirecting the probe beam towards a quadrant photodetector. This detector is better suited to sense the AC oscillation of the probe beam along the y-axis by partitioning the beam into four segments and evaluating the ratio of the converted electrical signals from each quadrant. Furthermore, in the PD setup, the probe and pump do not intersect at the same point. Instead, the probe beam is offset along the y-axis to optimize the signal, which relies on both the deflection angle and the relative position of the detector to the beam.

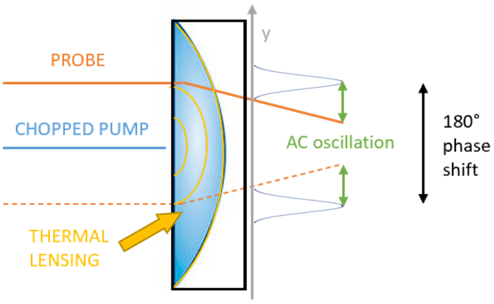

Figure 12: The chopped pump beam, upon impacting the sample, generates an AC thermal lensing effect due to heat diffusion in the substrate, which subsequently alters its refractive index. A probe beam passing through the sample at a different y-position than the pump beam will experience AC oscillation due to this lensing effect. In a uniform sample with an appropriately aligned setup, symmetry in the distribution of the detected AC signal around the point of pump beam impact is both expected and observed. Additionally, a phase shift of 180° is noticeable between these two signals, when tested.

It's crucial to emphasize that uniform absorption across a sample should not be presumed without careful consideration. The sample's surface may be riddled with various types of defects, each with its unique properties. As a result, the ability to predict the Photodeflection signal distribution with precision diminishes, and symmetry around the pump crossing point cannot be guaranteed. Even the status of the crossing point as a local minimum could be questionable.

These implications become particularly visible when alternating between the two experimental setups while keeping the pump alignment on a defect. The existence of an AC modulation signal is a consistently observed phenomenon across both setups, regardless of

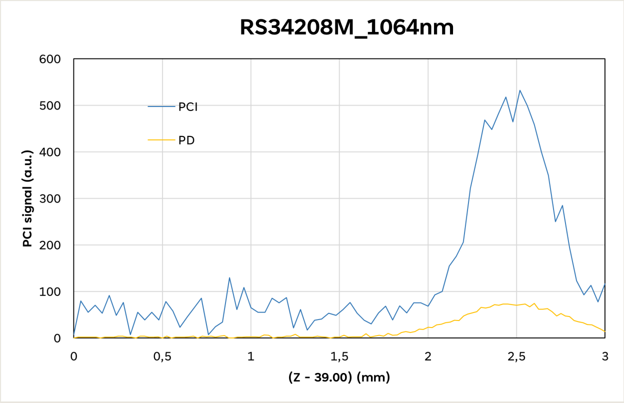

Figure 13: A Z-scan comparison of a uniform region for both techniques is shown here, highlighting an approximate 10:1 ratio between the signals. RS34208M_1064nm is the identifier for the AlGaAs sample.

whether the pump and probe are separated. However, the amplitude of this signal may or may not peak with minor adjustments to the stage position. This unpredictability is attributable to the potentially complex morphology and intrinsically unpredictable nature of the sample's coating defects, which may exceed the simple geometry of a point absorber. In these scenarios, Equation 12 needs to be adapted as shown below, under the assumption that an absorber can be modeled as a small point defect relative to the pump beam waist - thus disregarding its real and potentially macroscopic shape-. Both scenarios are illustrated in Figure 14.

$$\Theta = \frac{1}{n}\frac{dn}{dT}\frac{1}{\kappa}\frac{P}{\pi w_p}\frac{2R_{abs}^2}{w_p^2} \tag{13}$$

where R_{abs} denotes the radius of an opaque spot that absorbs the same power as the absorber.

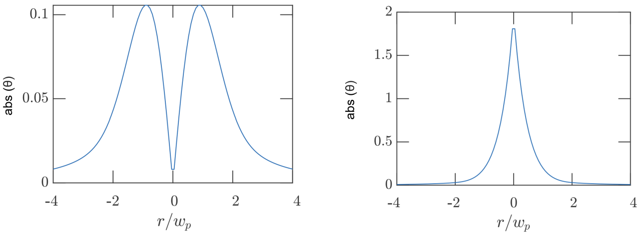

(a) Uniform region.
(b) Point absorber.

Figure 14: Theoretical plots illustrating the amplitude of the deflection angle, derived from Equation 13, are shown for a uniformly absorbing region (left) and for a point absorber (right). In this context, *r* represents the distance between the centers of the pump and probe beams.

4

INVESTIGATION OF ALGAAS COATINGS

The experimental setup delineated in Chapter 3 was employed for the characterization of Aluminum Gallium Arsenide (AlGaAs) coatings, specifically designed for LIGO mirrors. The setup and measurement technique was adapted to investigate the underlying physics and the nature of defects identified via the PCI signal.

4.1 ALGAAS: A HIGH-PERFORMANCE NEAR-INFRARED (NIR) COATING

Mirror coatings are pivotal in a multitude of scientific and technological applications, encompassing high-precision frequency stabilization of lasers, GW detection, and quantum optomechanics. Among various mirror coatings, AlGaAs coatings have earned substantial interest owing to their distinctive properties and potential applications.

AlGaAs mirror coatings comprise a compound semiconductor material, facilitating the generation of arbitrary stacks of high-index-contrast materials while preserving near-perfect crystalline order. This results in significant enhancements in the achievable mechanical quality factor, a metric indicative of the energy loss per oscillation cycle (i. e., the inverse of mechanical loss). Given the impact of the dangling bonds typically encountered in amorphous dielectric materials such as Ta_2O_5, the utilization of a single-crystal mirror stack like AlGaAs should permit a substantial reduction in the dissipation, while preserving excellent reflectivity.

A study conducted by Garrett D. Cole et al. [9] presented high-performance micromechanical megahertz oscillators predicated on freestanding monocrystalline $Al_xGa_{1-x}As$ distributed Bragg reflectors . In comparison with dielectric reflectors, the low mechanical loss of the monocrystalline heterostructure leads to significant improvements in the achievable mechanical quality factor Q while concurrently exhibiting near unity reflectivity. Experimental characterization yields an optical reflectivity of over 99.98% and mechanical quality factors up to 20,000 at 4K. This materials system is not only a compelling candidate for optical coatings with ultralow thermal noise [10], but also provides a promising path towards quantum optical control of massive micromechanical mirrors.

A Distributed Bragg Reflector (DBR) is an optical device engineered to achieve high reflectivity at designated wavelengths. This is accomplished by stacking periodic layers of materials, each possessing distinct refractive indices, in an alternating sequence.

The concept delineated in the study seeks to improve on previous works by fabricating the oscillator directly from a single-crystal Bragg reflector. The employment of compound semiconductor materials such as GaAs and related alloys allows for the generation of

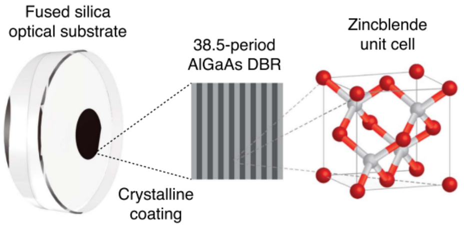

(a) A schematic representation of a crystalline supermirror, comprising a super-polished fused silica substrate with a substrate-transferred NIR crystalline coating. The first inset illustrates the repeating and alternating high-index GaAs and low-index $Al_{0.92}Ga_{0.08}As$ layers, while the second depicts the zinc-blende unit cell constituting the coating.

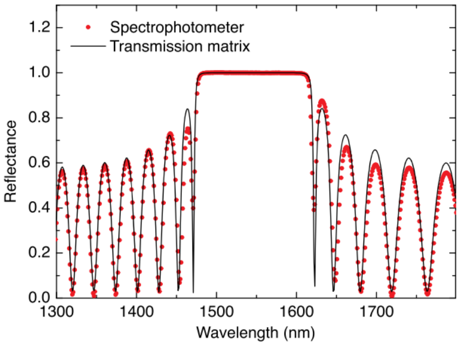

(b) The measured reflectance spectrum for a 38.5-period quarter-wave epitaxial multilayer with a center wavelength of 1550 nm. [10]

Figure 15

arbitrary stacks of high-index-contrast materials that maintain near-perfect crystalline order, resulting in significant improvements in the achievable mechanical quality factor.

In conclusion, AlGaAs mirror coatings offer a promising path towards achieving high-performance micromechanical oscillators with high reflectivity and mechanical quality factors. Their potential applications in various fields, including quantum optomechanics, make them an interesting area of research and development.

4.2 DEFECT ANALYSIS

This section focuses on a comprehensive examination of the inherent defects present in the mirror coatings through the precise quantification of their optical absorption. Each measurement result is analyzed to facilitate a better grasp of the intrinsic characteristics associated with the defects observed in the 1-inch diameter mirror sample. By evaluating the optical absorption data, valuable insights could be gained into the properties of these defects, thus contributing to a better understanding of the mirror coating performance. Notice that, for the purpose of this chapter, absorption values will be given in Arbitrary Units (AU), as what matters is the relative absorption of the mirror defects with respect to the baseline. Arbitrary Units are proportional to the PCI AC signal, hence to the absorption of the pump-crossed point on the sample.

4.2.1 *Mapping*

The optical configuration was aligned such that the surface was oriented perpendicular to the pump beam, achieved through a point absorption measurement of four distant points and subsequent angular compensation at the software level. Prior experiments had left visible damage on the sample surface; hence, the area designated for mapping was consciously placed as remote as possible from these damaged sections. This was done to mitigate the possible impact of particulate matter, which might have originated from the disruption of upper layers, on the absorption values of the unaffected regions. The 1064 nm He-Ne laser was kept at 120 mW by means of the half-wavelength plate for all the scans.

A square region spanning 8-by-8 mm (refer to Figure 16) was subjected to examination, deploying 8 mm-long x-directional scans with incremental steps of 25 μm. Each line was distanced from its neighbor by 50 μm along the y-axis. Consequently, this procedure generated a raster-scan of an array incorporating a total of 6400 points. The ensuing data were processed using Excel to construct a visual representation of the area in terms of the PCI signal recorded at each point.

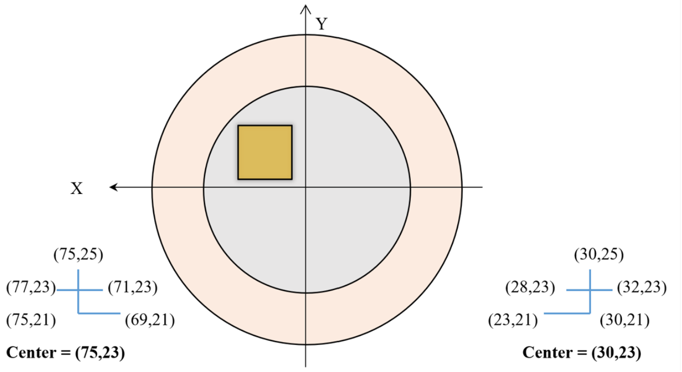

Figure 16: Schematic representation of the sample with the mapped area highlighted in yellow. The markings displayed on the left and right of the image are etched on the sample holder and serve as a reference for the location of peaks, whose coordinates are rigorously stored with respect to this frame.

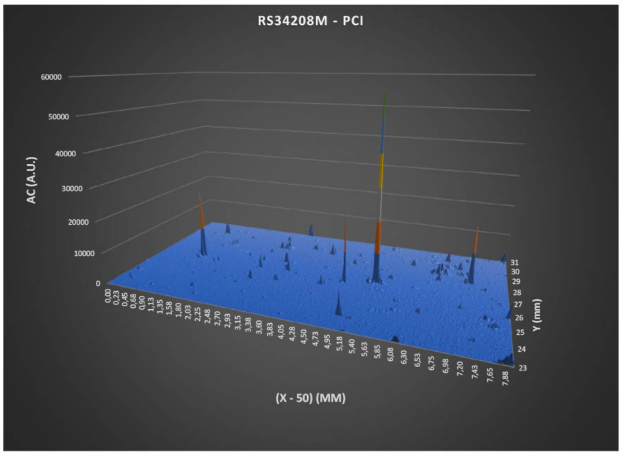

(a) Scale adjusted to 60,000 AU to emphasize the most prominent peaks.

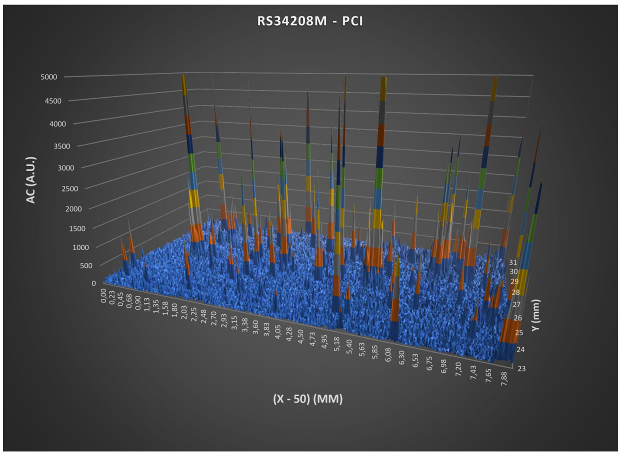

(b) Scale adjusted to 5,000 AU to remove outliers and enhance the background.

Figure 17: The 3D plots are obtained by graphing the PCI signal in arbitrary units (AU) for each pair of coordinates.

In particular, Figure 17 depicts a background characterized by a low PCI signal - a trait congruent with the expected behavior for low-absorption mirrors - along with a noisy phase. As detailed previously, the phase tends to stabilize at the calibrated value in the presence of absorbing point defects. Over the course of the scan, more than 200 defects of uncertain and likely diverse nature were identified. The interpretation of the observed phenomena is supported by the signal's phase behavior. The presence of significant absorption, coupled with a phase that stabilizes at a value divergent from the anticipated one, implies a defect of a more complex nature than a mere absorber, potentially a scatterer. Furthermore, it is crucial to consider the potential influence of surface contaminants, such as dust particles and various absorbed molecules, which could contribute to some of these observed defects. A more comprehensive explanation of these interpretations, including potential causes and their implications, will be addressed in the forthcoming subsections.

Upon completion of the initial measurements, PCI was executed on the reverse side of the sample. This methodology allows for the evaluation of absorption within the multi-layered mirror from the perspective of the fused silica substrate. Given the different refractive index of the substrate compared to air, a slight realignment was needed to accommodate for the consequent shift in the Rayleigh range by a few millimeters. This adjustment was implemented through the utilization of a motorized stage to move the detector. However, the backside of the sample did not yield a significant signal, suggesting that the absorption at this location is likely below the detection threshold of our system. This finding is contrary to our expectations based on the manufacturing process (additional details in Figure 18).

Figure 18: The layered mirror structure is initially grown on a GaAs substrate. Following this, the mirror coating is separated, inverted, and positioned on an optically fused silica substrate. This process is informed by the fact that optical absorption primarily occurs in the initial few layers exposed to the laser, and the top layers grown are anticipated to be of lower quality. An instance justifying this assumption involves the potential growth of a pyramidal-shaped crystalline defect through the layers, which could initiate in the first layer and expand significantly towards the end of the deposition process. Particularly in the case of AlGaAs, the formation of a crystalline Aluminum cluster could serve as a point absorber for the mirror.

One last takeaway is that the DC probe transmission value tends to increase, in each x-line scan, as the crossing point moves in the positive direction, demonstrating non-uniformity in the coating, with the left side of the mirror being more transmitting (thus less reflective) than the right side (see Figure 20).

4.2.2 *Characterization of Peaks*

As hinted earlier, understanding the nature of a specific defect requires more than just the AC PCI signal. Hence, it is essential to consider both the DC transmission of the probe and the phase shift between probe and pump waves.

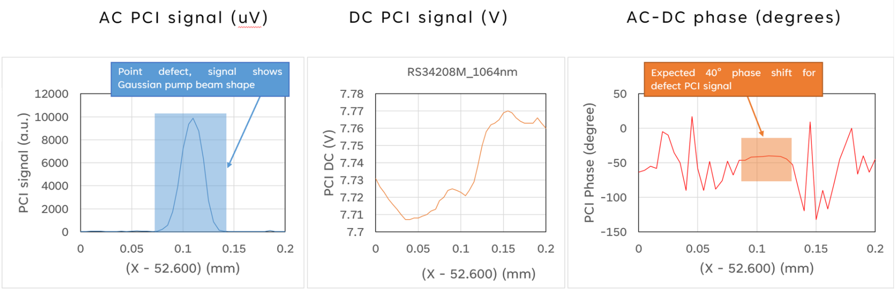

Figure 19: An X-scan of a simple point absorber, demonstrating the AC signal — that is, the modulation of the central peak of the self-interference pattern of the probe —, the DC signal, and the phase. The chosen X-step for the scan is 5 μm, which provides sufficient resolution to capture the Gaussian shape of the pump beam, indicating that the defect is likely smaller than the pump beam waist. The DC value fluctuates within a range commensurate with the expected uncertainty, implying that the defect does not significantly impact the probe transmission. Ultimately, at the peak, the phase stabilizes around the calibrated value, as expected for a basic absorbing defect.

The defect represented in Figure 19 is typical in nature, though most defects exhibit a much lower relative absorption (approximately 300-400 AU). However, as previously noted, a number of defects display different behaviors, which suggest varying characteristics of the defect point. A case in point is illustrated in Figure 20. Here, (a) depicts a roughly 5% dip in the probe transmission through the mirror; this could indicate a scattering defect, where a portion of the laser beam might be scattered in various directions, thereby reducing the amount reaching the detector. Interestingly, the outcome remains essentially unchanged regardless of whether the pump is incident on the sample, substantiating that the observed effect is not associated with pump-induced absorption. (b) portrays the phase of the defect, which differs from the anticipated value of approximately -40° for thermal defects. (c) presents the mirror when the crossing point is aligned on the scattering defect: the IR viewer accentuates the laser being scattered in various directions by the defect.

To conclude this subsection, it is noteworthy to demonstrate that defects can exhibit a highly intricate structure, extending in both x and y directions, as portrayed in Figure 21a. The origin of such an extensive absorbing cluster could be attributed to multiple defects of varying nature converging around a nucleus. This underscores the inadequacy of a singular physical model in fully explaining the properties of this mirror. Another situation of interest is demonstrated in Figure 21b, where, along the defective line, the phase transitions from -40° to -20°. In this case, one could assume the convolution of two

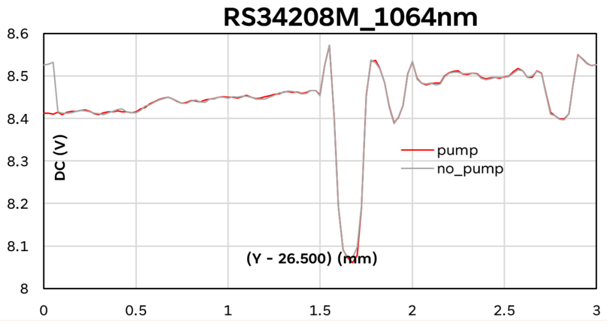

(a) DC line scan, with pump alternatively blocked and active.

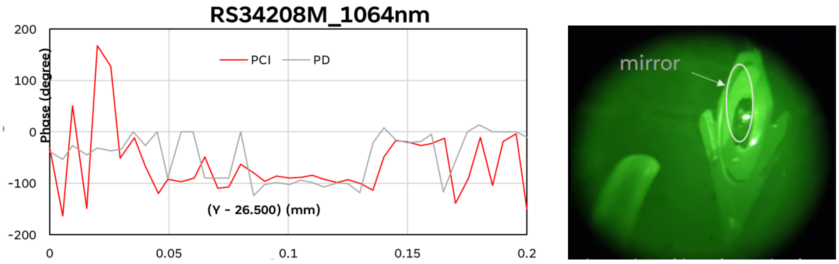

(b) Phase line scan for both PCI and PD setups.

(c) Image of the defect captured with an IR viewer.

Figure 20: Analysis of a defect exhibiting scattering behavior.

distinct peaks, one less absorptive than the other, but whose phase influences the overall phase of the probe signal.

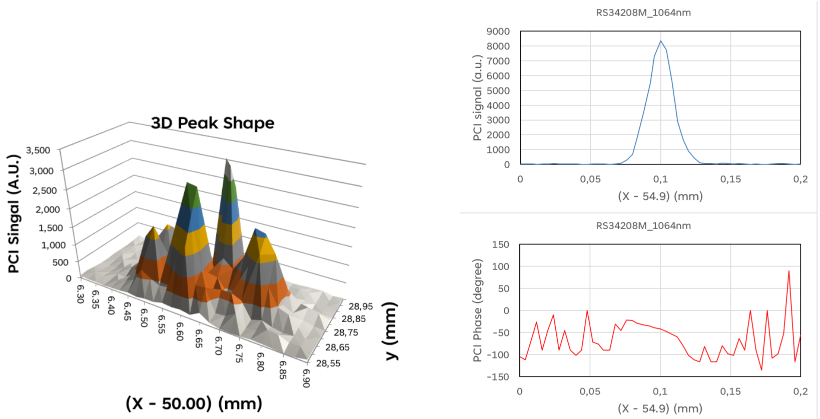

(a) 3D map of PCI AC signal for a complex defect.

(b) Convolution of 2 defects in close proximity.

Figure 21: Graphical representations of more intricate defects.

4.2.3 *Power dependent measurements*

For a more comprehensive understanding of the optical absorption of the mirror, it is crucial to consider that an increased pump power might trigger defects with energy levels residing within the forbidden bandgap of a semiconductor (such as Gallium Arsenide), thus rendering it sensitive to wavelengths that would normally pass through unaffected. This phenomenon can lead to a perturbation in the thermal properties of the material, consequently giving rise to non-linearities in optical absorption. Therefore, it is postulated that higher pump power levels should correspond to increased absorption - this is to be interpreted in the context of possible non-linearities intrinsic to the photodetector itself. As Figure 22 demonstrates, this hypothesis seems to hold true for regular points.

The execution of these measurements with the available setup requires a sequence of steps:

1. Initially, the sample is retracted from the path of the pump beam via a motorized stage, thereby enabling a direct route from the pump beam to a power detector.

2. Subsequently, the half-wave plate is manipulated to modulate the power. It is crucial to provide sufficient time for the power detector to accurately respond to these alterations.

3. The sample is then re-positioned back to its original location utilizing the LabView interface to control the piezo stage. This action ensures the intersection point aligns with the defect under investigation.

4. Lastly, using real-time sampling with adequate averaging (i. e.noise filtering), a sufficient duration is allowed for the signals to stabilize and attain the sought value.

Nevertheless, for the majority of defects, the observed behavior does not conform to this straightforward theoretical expectation. On the contrary, power-dependent measurements often indicate a downward trend, suggesting lower absorption with increased pump power. This trend is apparent in both thermal absorbing and scattering defects, which suggests that it's likely to hold for combinations of the two as well (see Figure 23). One significant observation is that, during these measurements, non-linearities are less noticeable in Photodeflection (PD) setup. If we were to accept the hypothesis of free-carrier generation, one plausible explanation could be that the diffusion length of these carriers is comparable or shorter than the separation between the two laser beams, resulting in a less pronounced effect on the deflection of the probe.

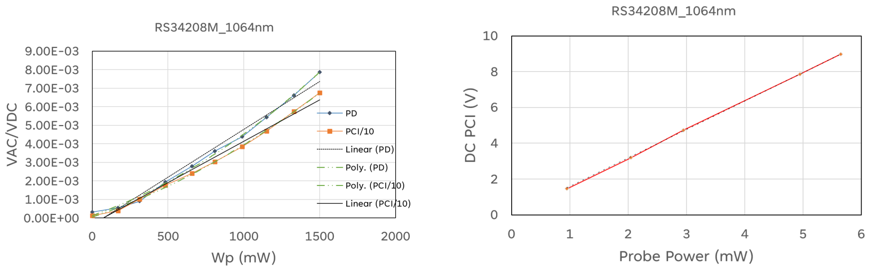

(a) Measurements conducted utilizing both Photodetector and Photo-thermal Common-path Interferometry methodologies.

(b) Evaluation of detector linearity via modulation of probe power and subsequent measurement of the corresponding transmitted power impinging on the detector.

Figure 22: Measurement dependent on power intensity conducted on a regular point.

Furthermore, the validation of pump-induced absorption might be achieved by utilizing the Photo-thermal Common-path Interferometry (PCI) apparatus. However, instead of focusing exclusively on the central fringe, the comprehensive interference pattern is captured. As expounded in Chapter 3, the PCI configuration is designed in such a manner that the photodetector accumulates the power from the central fringe. The intensity of this fringe is modulated due to the initiation of self-interference from the chopped pump beam interacting with the sample. Nevertheless, the total transmitted probe power through the sample should remain unaffected by the thermal lensing effect. Therefore, by removing the integrated iris from the photodetector and employing an additional convex lens to focus the complete interference pattern, or in other words, the whole beam onto it, one should anticipate no modulation, hence, no AC signal, excluding the pump instigating probe-power absorption in the sample. The constraints of the setup rendered it impracticable to focus the entire beam within the detector, yet a significant outcome, as illustrated and elucidated in Figure 24, was still achieved. For both scenarios, the setup was calibrated to accumulate identical DC probe power, thereby enabling a direct comparison of the AC signals.

4.2.4 *Damage through Defects*

The primary concern uncovered when employing the PCI setup with the aforementioned AlGaAs mirror is the likelihood for the pump power to induce damage in the layer, specifically in correspondence with the absorbing defects. This same sample was previously analysed using a spatially-resolved *ringdown* system, yet no points were found to be damaged. This system comprises a laser that oscillates between a high-quality mirror and a semi-transparent one, travers-

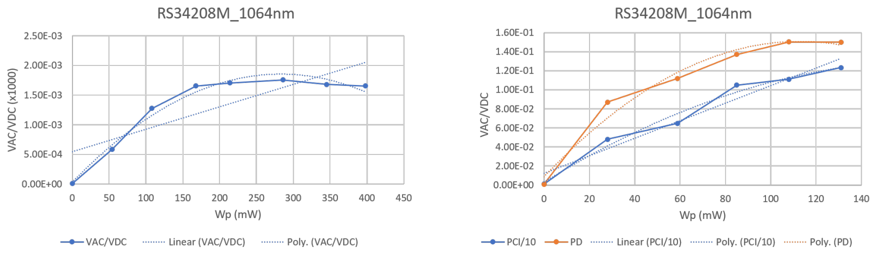

(a) Modulation depth of thermal defect (refer to Figure 19) measured using PCI setup.

(b) Modulation depth of scatterer defect (refer to Figure 20) measured using both PD and PCI setups. The PCI signal is divided by 10 for comparison (as previously explained, the PD signal is expected to be roughly an order of magnitude lower than the PCI's).

Figure 23: Power-dependent measurements of two distinct defect types.

ing the sample twice per cycle. The beam transmitted by the semi-transparent mirror is captured by a photodetector which measures the incident power. Upon turning off the laser, the signal gradually diminishes, and the rate of its decay is proportional to the optical absorption of the mirror. However, this system utilizes a substantially wider beam waist, implying that the power per unit area, and consequently the power impacting the defects, will be diminished. Furthermore, the total absorption measured will be averaged over the whole illuminated area, where the ratio of defects to regular points is intrinsically low.

When executing power-dependent measurements with both PD and PCI setups, the laser beam power is typically stopped around 500 mW, which equates to subjecting the sample to an intensity of roughly $12kW/cm^2$, given the pump beam waist. This power density is apparently sufficient to damage the mirror layers if an absorbing defect is present. To establish a threshold laser beam power value that ensures the LIGO interferometer operates without damage when these types of mirrors are utilized, the absorption coefficient of the defect itself must be considered. Naturally, this value is dependent on the specific defect, which is inherently unpredictable. As a result, the deposition process likely requires further enhancements before it becomes viable for LIGO's project, given that the damage produced by these operations appears to be irreversible (refer to Figure 25a).

Moreover, inspecting the sample from the rear side (Fused Silica) through a microscope enabled us to strengthen the hypothesis on the phenomena revealed by power-dependent measurements. Figure 25b presents the appearance of a damaged point as observed from the backside, while Figure 26 reveals that numerous points exhibiting the same visible diffraction pattern are dispersed across the surface.

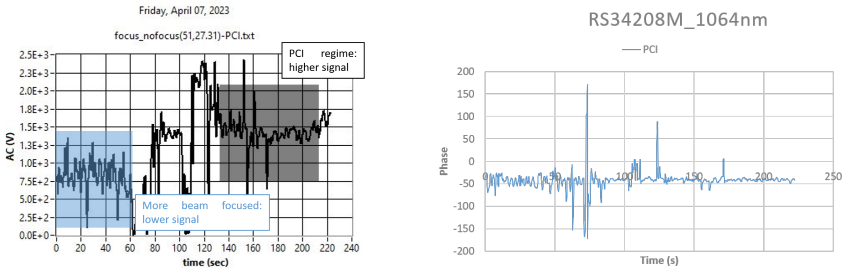

(a) AC signal measured under two conditions: the region delineated in blue depicts the time-dependent signal following the focusing of a larger fraction of the beam onto the detector, while the region marked in black corresponds to the signal measured under conventional PCI conditions. The interlude between these two regions is meaningless, as the setup was being reconfigured during this time.

(b) Phase signal gathered throughout the entire duration of the measurement and setup switching.

Figure 24: These diagrams indicate that concentrating a more substantial section of the probe beam's self-interference pattern onto the detector reduces the modulation attributable to the chopped pump. This is expected in the case of a thermal defect, as the lateral fringes of the interference pattern negate each other, thereby diminishing the total power striking the detector. However, since focusing the entire beam was unattainable, this information alone is inadequate to completely exclude the possibility of pump-induced absorption. However, the phase remained consistent throughout the procedure, suggesting that the absorption measured is indeed thermal. If the pump were modifying the electronic structure of the material, inducing the creation of free carriers, the phase of the AC modulation produced would be approximately 180°, as the generation mechanism is much faster than the diffusion of the thermal wave.

Consequently, it is reasonable to assume that all these points have incurred damage from the PCI measurements, but not to an extent that would compromise the integrity of the mirror. Areas subjected to such effects are evidently predisposed to non-linearities and, in general, unpredictable behavior, providing a plausible explanation for the downward trend detected in every defect analyzed.

4.3 FINAL REMARKS

In summary, the comprehensive evaluation of the AlGaAs mirror through PD and PCI methods has explicated relevant features that bear implications for the mirror's functionality and suitability for LIGO applications. While these findings significantly contribute to

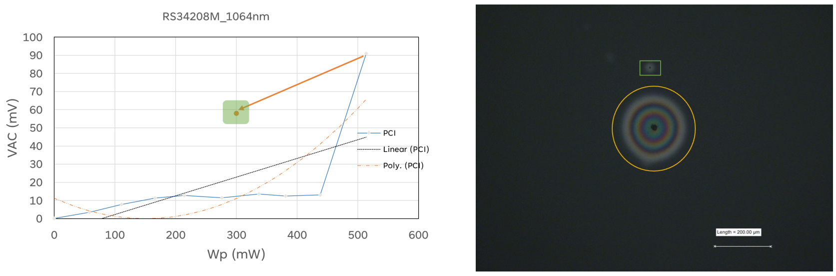

(a) A drastic increase in the PCI signal value at 514 mW (which was noticed after approximately 30 seconds) indicates that damage has occurred. Reassessing the signal for a lower pump beam power after a rest period confirms that the damage is indeed irreversible.

(b) Photograph of the defect viewed from the backside. The annular diffraction pattern illustrates how the laser was able to gradually penetrate through the mirror layer by layer, consequently creating a cone-shaped hole in the sample.

Figure 25: Illustration of a damaged point where the laser has compromised all layers of the mirror.

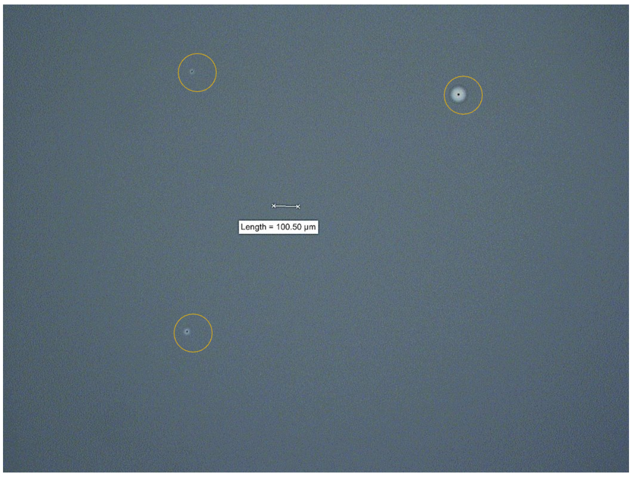

Figure 26: This photograph, captured from the rear side of the sample, reveals multiple impacted points. The same conical shape discussed in Figure 25b is apparent, supporting the direct correlation between the damage to the mirror layers and the power-dependent measurements conducted on the sample.

our understanding of the mirror's performance as an ultralow absorption material, they simultaneously underscore the necessity of refining manufacturing methodologies to curtail the prevalence of such defects.

A particularly noteworthy discovery of this investigation was the mirror layers' vulnerability to thermal damage when subjected to elevated pump power levels. This susceptibility calls into question the long-term durability and operational stability of the mirror in high-intensity applications, such as those demanded by the LIGO project.

Consequently, it insinuates the potential necessity of advancements in deposition procedures and material selection to increase resistance against intense laser irradiation. Moreover, the study identified regions displaying nonlinear and unpredictable behavior, suggesting a disturbance caused by the PCI measurements. Despite these areas remaining structurally intact, their altered characteristics might negatively impact the overall performance of the mirror.

To sum up, this investigation accentuates the imperative for ongoing advancements in mirror fabrication and evaluation procedures to fulfill the rigorous performance requisites stipulated by applications such as LIGO.

Part III

MECHANICAL LOSS AND OPTICAL ABSORPTION IN AMORPHOUS BINARY OXIDE COATINGS

The LIGO Scientific Collaboration has identified a unique blend of titanium dioxide ($\mathrm{TiO_2}$) and germanium dioxide ($\mathrm{GeO_2}$), which exhibits ultra-low internal dissipation at the level of 10^{-4} [26]. This remarkable property offers the potential for nearly a twofold enhancement in Brownian noise performance compared to state-of-the-art materials, such as alternating layers of tantalum pentoxide ($\mathrm{Ta_2O_5}$) and silica. Currently, a composition consisting of 44% $\mathrm{TiO_2}$ and 56% $\mathrm{GeO_2}$ in the high-refractive-index layers of the interferometer mirrors is under investigation as the most promising candidate to meet LIGO's operational requirements. This advancement marks a significant step towards the development of mirrors that satisfy the thermal noise specifications for the proposed upgrades to the Advanced LIGO detectors.

In the following section, an innovative cryogenic setup is detailed. This apparatus is specifically designed to carry out temperature-dependent measurements of the amorphous oxide coating materials across various frequencies. This allows for an exploration of a frequency range more aligned with LIGO's operational point, enhancing the time efficiency of existing multi-frequency measurement configurations.

Lastly, utilizing the setup outlined in Chapter 3, optical absorption measurements will be conducted on the same samples, furnishing a comprehensive understanding of the performance of these amorphous coating materials for LIGO's mirrors.

5

EXPERIMENTAL SETUP AND MODELING OF THE RESONATORS

5.1 MECHANICAL LOSS MEASUREMENT AT RESONANT MODES OF COATINGS

A high-quality test mass is usually characterized by a very low mechanical loss, making it challenging to measure at any arbitrary frequency. Therefore, measurements are usually conducted at the system's resonant frequencies to maximize the detectable oscillation amplitude and thus the setup's sensitivity to mechanical loss. The mechanical loss of the resonant mode, characterized by its angular resonant frequency ω_0, is defined as follows:

$$\phi(\omega_0) = \frac{E_{\mathrm{dissipated}}}{2\pi E_{\mathrm{stored}}}, \tag{14}$$

where $E_{\mathrm{dissipated}}$ represents the energy dissipated or lost within each oscillation, and E_{stored} corresponds to the total energy stored in the vibrating system. Mechanical loss can be assessed by observing the decay of the amplitude *A* of the resonant oscillation in free motion, and subsequently extracting the time constant of the exponential decay:

$$A = A_0 e^{-\frac{\phi(\omega_0)\omega_0 t}{2}}. \tag{15}$$

When the test mass is coated with a specific coating for which the mechanical loss needs to be determined, the mechanical loss of the coating can be extracted from the losses of both the substrate and the coated sample [11]. This process can be articulated as:

$$\phi(\omega_0)_{\mathrm{coated}} = \phi(\omega_0)_{\mathrm{substrate}} + \frac{E_c}{E_s}\phi(\omega_0)_{\mathrm{coating}}, \tag{16}$$

where $\frac{E_c}{E_s}$ is the ratio of the energy stored in the coating to the energy stored in the substrate. This energy ratio is dependent on the mechanical structure and the materials of the sample. For complex sample shapes, these values can be computed from a Finite Element Method (FEM) simulation on software such as COMSOL® (refer to section 5.3.1 for further details).

5.2 PERFORMING TEMPERATURE-DEPENDENT MECHANICAL LOSS MEASUREMENTS

Recent studies suggest that germanium dioxide (GeO_2)-based films are among the most promising materials for room-temperature Gravitational Wave Detectors. The mechanical loss of undoped GeO_2 films at room temperature is significantly lower than any other known amorphous oxides, excluding silica (SiO_2) [26]. This has led to exploring the potential of substituting the current titania-doped tantala ($Ti:Ta_2O_5$) layers with those based on GeO_2.

Given that SiO_2 is used as the low-index layer (with a refractive index of 1.45 at a wavelength of 1064 nm), it is necessary to increase the refractive index of GeO_2 (which is 1.65) with suitable dopants. This strategy aims to reduce the number of layer pairs required for achieving the needed reflectivity, thereby realizing lower total mechanical loss in multi-layer films.

Coatings based on SiO_2 and titania-doped germania (44% $Ti:GeO_2$) films, with a refractive index of 1.88, are predicted to halve the room-temperature thermal noise relative to that of the current Advanced LIGO coatings. Such a reduction would meet the design target for the Advanced LIGO Plus (A+).

5.2.1 *Experimental Setup*

The constructed experimental setup, illustrated in Figure 27, comprises three main components:

A. **Optical Setup** (middle): This component is employed to align three Super Luminescent Diode (SLD) beams accurately, enabling them to illuminate three different resonators. It also collects the reflected beam using the same quadrant photodetector.

B. **Cryostat Control** (right): This component generates the capacitive driving force, responsible for exciting the resonators at their resonant frequencies. It also helps stabilize the temperature at each measurement step.

C. **Detection Instruments** (left): This section captures and analyzes the laser signal.

OPTICAL SETUP The optical setup employs an SLD operating at a wavelength of 1.5 μm. The SLD, a semiconductor device that emits broad-spectrum light similar to a Light Emitting Diode (LED) but with higher optical power and a relatively wider emission bandwidth, is favored over a standard laser source due to its small coherence length. A coherent beam, reflecting on the top and bottom surfaces of

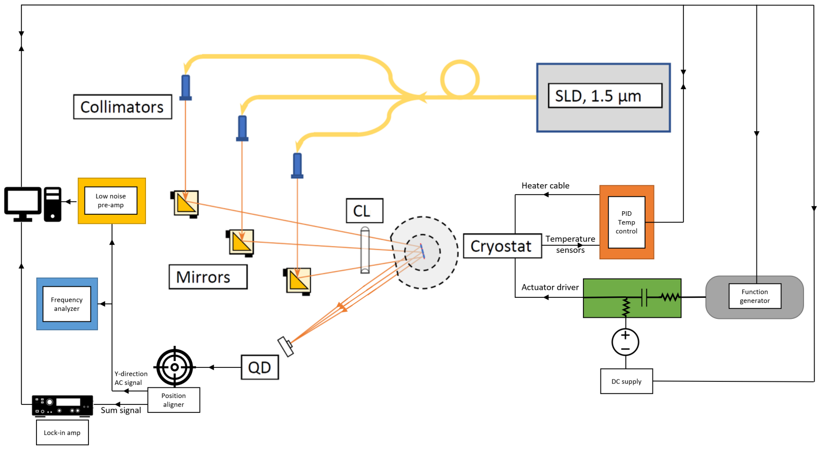

Figure 27: Mechanical loss setup.

the resonator (separated by only 100 µm), could interfere with itself and nullify the signal.

The SLD beam traverses a fiber beam splitter, which partitions the signal into four fiber cables. Owing to the inherent variability in the power output, the central fiber cable exhibits an output that is approximately 30% greater than its lateral counterparts. To mitigate the potential overshadowing effect of its elevated optical noise on the oscillations from the adjacent beams, a Neutral Density (ND) attenuating filter is positioned along its trajectory. This ensures balanced signal discernibility across all channels. The three employed beams are fed into three adjustable collimators. These collimators, together with the three mirrors directing the beams towards the cryostat, can be finely adjusted in both the x and y directions. This offers enough degrees of freedom to achieve the correct alignment of the beams, ensuring that all the reflected beams are collected by the detector. As a result, the oscillations of all three resonators used in this experiment can be recorded.

A cylindrical lens, adjusted to have its focal plane on the detector, is strategically placed along the beam's path to constrict the light in the y-direction. This arrangement minimizes the likelihood of the detector picking up beams reflected from different parts of the cryostat, while enhancing sensitivity in the y-direction, as desired. Even if such off-target beams are collected, their intensity is invariably lesser than that of the primary beams reflected by the sample.

PID stands for Proportional, Integral, Derivative. It's a type of feedback controller whose output, a control variable, is based on the error between a desired setpoint and a measured process variable.

CRYOSTAT CONTROL The utilized cryostat comes equipped with three feedthroughs for multiple elements. Specifically, three temperature sensors are placed at three distinct points on the sample holder (refer to Figure 28). These sensors, connected to a PID temperature controller, monitor temperature stability around the sample area. The controller reads the temperature cooled by the liquid helium/nitrogen flow and tunes a resistive heater to stabilize the temperature around the desired value. The PID parameters are primarily determined by the controller, based on the performance of the heater and the transfer tube feeding the cryogenic liquid from the dewar to the cryostat.

A cryogenic dewar is a highly insulated container used to store and transport materials at extremely low temperatures. It is commonly used for handling and preserving cryogenic liquids and gases.

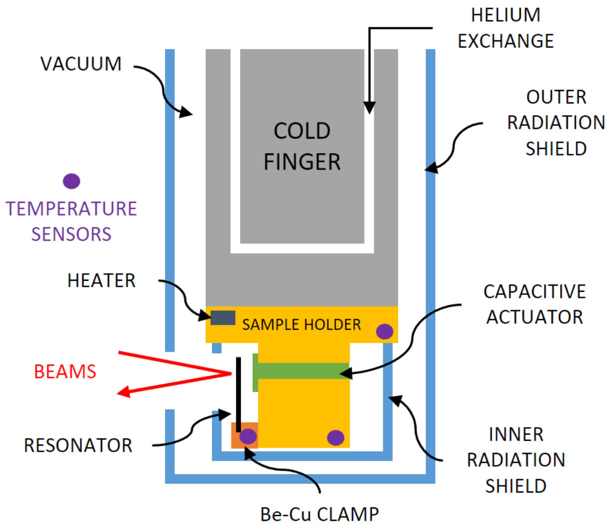

Figure 28: Schematic of the sample holder inside the cryostat. The *cold finger* is in contact with the liquid helium/nitrogen flow, while the resonator chamber is insulated and vacuum-pumped to enhance the quality factor of the resonant modes and prevent ice formation on the resonator. Two aluminum radiation shields are utilized to minimize environmental electromagnetic wave interference with the capacitive driver.

The quality factor (Q-factor) of a resonant mode is a measure of the resonance system's efficiency and selectivity. In the context of resonance, it describes the sharpness or narrowness of a resonance peak in a frequency response curve, representing the inverse of the mechanical loss.

The actuator, affixed to the sample holder and soldered for external connection, is powered by both AC and DC signals. The DC component comes from a high-voltage DC power supply, while the AC component is generated by a function generator, which allows adjustment of the waveform, amplitude, and frequency. Both signals pass through a filter that cleans the electrical input and decouples any DC component from the function generator. The necessity for both DC and AC components is to maintain a linear relationship between the electrostatic force exerted on the resonator and the amplitude of the input waveform. Indeed, the Coulomb force, which is $F = \frac{CV^2}{2d}$ and thus proportional to the square of the applied voltage, is expressed as:

$$\begin{aligned} V^2 &= [V_{DC} + V_{AC}\sin(\omega t)]^2 = \\ &= V_{DC}^2 + 2V_{DC}V_{AC}\sin(\omega t) + V_{AC}^2\sin^2(\omega t) \end{aligned} \tag{17}$$

By setting $V_{DC} \gg V_{AC}$, the V_{AC}^2 component, which is proportional to $2\omega t$, becomes negligible, and the total force becomes linearly proportional to the AC component, as desired.

The cryostat sample chamber is pumped using a vacuum station, consisting of a membrane pump and a turbomolecular pump in series, capable of achieving vacuum levels around 10^{-7} bars. Simultaneously, a separate rotary pump drives another line to transport the cryogenic liquid from the dewar through the cryostat. The transfer tube connecting the dewar to the cryostat also needs to be pumped to prevent room heat from vaporizing the cryogenic liquid.

(a) The capacitors are each coupled to one of the three different resonators and stimulated with the same signal to excite the resonant modes.

(b) The resonators are firmly held using a Be-Cu clamp and permitted to oscillate in the z-direction. This motion leads to y-direction oscillations of the laser beam striking the resonators. The top screw is fastened using a carefully controlled torque of $\sim 0.05 \mathrm{N} \cdot \mathrm{m}$.

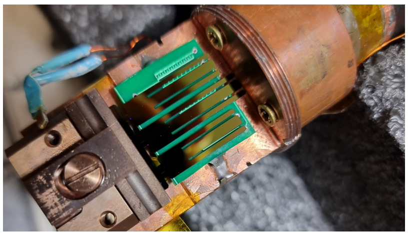

(c) The spacing of the available PCB capacitors does not precisely match that of the resonators. However, when affixing the clamp to the Be-Cu holder, it is advisable to position the actuators slightly off-center from the tridents. This positioning aids in enhancing the excitation of anti-symmetric modes.

Figure 29: Images showcasing the sample holder components employed for the specific resonators in this experiment.

Material selection for the sample holder, clamp, and soldering wires is crucial for cryogenic experiments. Beryllium:Copper (5%) is an excellent material for low-temperature measurements due to several advantageous properties, including:

- High strength and ductility at low temperatures

- High thermal and electrical conductivity, desirable for cooling down
- Absence of magnetic interference, ensuring reliable electronics performance and preventing magnetic volumetric effect. In contrast, INVAR exhibits high thermal expansion effects at low temperatures.

INVAR is a type of austenitic stainless steel, known for its unique properties of having a very low coefficient of thermal expansion at room temperature.

For soldering, indium replaces the more common tin, as tin undergoes a crystalline phase transition and becomes powdery at around 223 K.

DETECTION INSTRUMENTS The signal from the quadrant photodetector undergoes initial processing through a position aligner, which is utilized to finely center the beams on the detector and thereby maximize the detection sensitivity of the oscillations. The total intensity impinging on the detector, referred to as the sum signal, is then fed into a lock-in amplifier for alignment monitoring. Concurrently, the AC signal in the y-direction is routed to both a frequency analyzer and a low-noise pre-amplifier.

The frequency analyzer performs a Fast Fourier Transform on the signal, producing a plot along the frequency axis. This enables the identification of resonant modes and provides initial parameter settings. The low-noise pre-amplifier forwards the signal to a computer through a GPIB interface for data collection.

All experimental procedures are coordinated through LabVIEW software, which is programmed to accomplish the following tasks:

A. Manage the temperature steps, which span from 295K down to 12K. The software also ensures adequate wait time at each temperature step to enable the chamber's temperature to stabilize, balancing the cooling effect of the cryogenic liquid and the heat compensation provided by the heater.

B. Establish the resonant modes and conduct a frequency scan around the anticipated values to identify peak responses. The software adjusts the range of measurements to account for any temperature-dependent shifts in resonant frequency.

C. Detect peaks by monitoring the measured oscillation amplitude around the expected frequency upon excitation. A peak is identified when the amplitude exceeds a set threshold, which is determined based on the amplitude of the peak in the previous step. This setup ensures that random spikes induced by external events do not inadvertently trigger a ringdown measurement.

D. Conduct the ringdown measurement by recording the amplitude as a function of time after the excitation is turned off. The measurement ceases when the amplitude has descended to 33% of the peak amplitude.

All the data is collected and analyzed through MATLAB, which extracts the mechanical loss from each ringdown by fitting a simple exponential curve and computing $\phi(f) = \frac{1}{\pi f \tau}$, according to Equation 15.

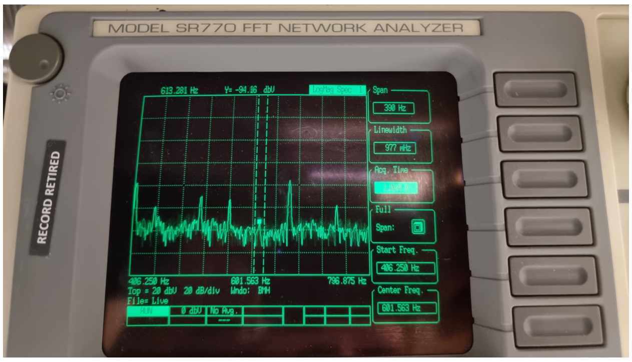

Figure 30: All high-quality modes excited for a single three-trident resonator, as shown in Figure 29b. Ideally, if the modes are not coupled to the base, one should not be able to excite any of the anti-symmetric modes by flicking a finger on the cryostat, an action that transmits a Dirac delta function of time (thus exciting all frequencies) through the base to the trident. If the clamp is tight enough, the anti-symmetric modes should not be excited, provided they have no torsional component.

5.3 THE RESONATORS

The design of suitable resonators for mechanical loss measurements aims to fulfill the main objective of providing multiple high-quality factor resonant modes at low frequencies. This ensures that the results for mechanical loss are consistent with the operational range of LIGO. Furthermore, the design should allow for reasonable ease of handling. The final design is depicted in Figure 29b, and the resulting modes are illustrated in Figure 30. The physical properties are analyzed using COMSOL®. Ideally, anti-symmetric modes are preferred, as they exert no torque on the clamp and thus are subject to reduced damping: a higher quality factor is anticipated. For these reasons, the group selected a trident shape, which demonstrates two anti-symmetric modes and is small enough that three of them with varying heights can be placed on the same base. This allows for a total of six enduring modes to be measured under ideal conditions.

5.3.1 *FEM simulations and design*

The FEM study aims at computing mainly two physical properties of the designed resonator:

- the **eigenfrequencies**, so that one can find the frequency range of the anti-symmetric resonant modes;
- the **elastic strain energies** stored in both the substrate and the coating for each mode, so that Equation 16 can be applied to the experimentally measured mechanical losses for the coated and uncoated samples and extract the loss of the coating, which is the ultimate goal.

ELASTIC ENERGY COMPUTATION For any given geometric structure subjected to a resonant frequency, the deformation across its surface varies as a consequence of the stored energy present in two predominant modes of the sample's motion:

1. *Bulk Elastic Energy*, E_{bulk}, represents the energy dissipation associated with volumetric deformations. It's computed by integrating over the geometry's volume, with the magnitude being contingent upon the material's bulk modulus, K, and the diagonal elements of the elastic Green-Lagrange tensor, denoted as S_{ii} or equivalently, θ:

$$E_{\text{bulk}} = \iiint \frac{1}{2} K \theta^2 dV. \tag{18}$$

2. *Shear Elastic Energy*, E_{shear}, pertains to the energy due to distortional (or shape) changes in the material. The quantification of this energy integrates over the volume of the structure, with influences from the material's shear modulus G and certain components of the S tensor:

$$E_{\text{shear}} = \iiint G \xi_{ij} \xi_{ij} dV, \tag{19}$$

with the ξ_{ij} terms derived from components of the strain matrix, S_{ijk}, modulated by the Kronecker delta function, δ_{ij}:

$$\xi_{i,j} = \frac{1}{2}(S_{ij} + S_{ji}) - \frac{1}{3}\delta_{ij}\theta. \tag{20}$$

The aggregate energy, either stored or dissipated within the geometry during deformation, is the summation of the aforementioned components:

$$E_{\text{total}} = E_{\text{bulk}} + E_{\text{shear}}. \tag{21}$$

For isotropic coatings, the formulations presented are pertinent. However, when addressing the Silicon substrate, an anisotropic material, a more intricate consideration is requisite, though the analysis of bulk and shear components may not be critical for material qualification, given that the mechanical loss of silicon is expected to be negligible with respect to that of the extracted coating loss.

The total energy, E_{total}, is articulated using a consolidated expression:

$$E_{\text{total}} = \frac{1}{2}\sum_{i=1}^{6} T_i S_i. \tag{22}$$

In this relation, the second-rank stress (**T**) and strain (**S**) tensors are encapsulated in the Voigt notation. The sequence (1, 2, 3, 4, 5, 6) corresponds to (*xx*, *yy*, *zz*, *yz*, *xz*, *xy*), which interlink through the stiffness tensor. Notably, the Voigt notation introduces a factor discrepancy for cross-coupled components relative to the traditional elastic theory. The components of the strain tensor can be explicitly characterized as:

$$\begin{aligned} S_1 &= \frac{\partial u_x}{\partial x} = \epsilon_{xx}, \quad \text{and similarly for } S_2 \text{ and } S_3; \\ S_6 &= \frac{\partial u_x}{\partial y} + \frac{\partial u_y}{\partial x} = 2\epsilon_{xy}, \quad \text{and similarly for } S_4 \text{ and } S_5. \end{aligned} \tag{23}$$

Resonating motion-induced deformations encompass both bulk and shear movements. Depending on the deformation profile of a resonating specimen, the relative energy distributions in E_{shear} and E_{bulk} can vary. Notably, for applications like gravitational wave detector mirror coatings, materials that predominantly dissipate energy via shear motion (orthogonal to the laser's sensing direction) will have a minimized contribution to coating Brownian thermal noise, rendering them more desirable.

In the COMSOL® framework, the elastic Green-Lagrange tensor can be accessed via '**solid.eel**' for Cartesian coordinates or through '**solid.eX/Y/Z**' for the material frame. Finally, '**solid.SX/Y/Z**' extracts the entries for the second Piola-Kirchoff stress tensor, preferred over the classic elastic stress tensor as it is referred to the material frame. The relevant evaluation formulas are detailed in Table 1.

MODEL GEOMETRIC SPECIFICATIONS AND ATTRIBUTES In constructing the 3D resonator model, the impact of wet etching on the vertices of the geometry is pivotal, primarily due to the intrinsic anisotropy of Silicon (elaborated further in Subsection 5.3.2). This specific feature is conspicuously evident from the photographic evidence presented in Figure 31. Consequently, the model's final geometric structure is delineated accordingly. The substrate, composed of Silicon, exhibits a thickness of 100 µm. Concurrently, the overlying coating measures (500 ± 20) nm in thickness. Given the distinct thermal attributes of the coating relative to the substrate, a bilateral coating of the resonators is recommended to prevent unintended bending during thermal reductions. However, there was an oversight during the deposition process by collaborating partners, resulting in a

QUANTITY	FORMULA
Bulk Energy	0.5 * solid.K * (solid.eel11 + solid.eel22 + solid.eel33)^2
Shear Energy	2/3 * solid.G * (solid.eX^2 + 3 * solid.eXY^2 + + 3 * solid.eXZ^2 + solid.eY^2 + 3 * solid.eYZ^2 + + solid.eZ^2 - solid.eY * solid.eZ - solid.eX * solid.eY + - solid.eX *solid.eZ)
Total Energy	0.5 * (solid.eX*solid.SX + solid.eY*solid.SY + + solid.eZ*solid.SZ + 2*solid.eXY*solid.SXY + + 2*solid.eXZ*solid.SXZ + 2*solid.eYZ*solid.SYZ)

Table 1: Formulas used to compute dissipated energy components for each mode on COMSOL®

unilateral coating of the first set of tridents. In the end, both measurements and simulations were performed on one-sided $\sim 500nm$ GeO_x and $Ti : SiO_x(66\%)$ coated tridents and double-sided $\sim 250nm$ $Ti : GeO_x(44\%)$ coated tridents. For material modeling, the elasticity matrices for coatings are derived from Young's modulus and the Poisson ratio, using Equation 24, provided by COMSOL® elasticity handbook. The exception is (100)-oriented Silicon, which is sourced from literature [29]; it follows the rules of cubic-crystalline materials, for which 2 degrees of freedom are not sufficient to express the elastic properties. For the amorphous coatings under consideration, their isotropic elasticity is represented in the stiffness matrix as:

$$\frac{E}{(1+\nu)(1-2\nu)}\begin{bmatrix} 1-\nu & \nu & \nu & 0 & 0 & 0 \\ \nu & 1-\nu & \nu & 0 & 0 & 0 \\ \nu & \nu & 1-\nu & 0 & 0 & 0 \\ 0 & 0 & 0 & \frac{1-2\nu}{2} & 0 & 0 \\ 0 & 0 & 0 & 0 & \frac{1-2\nu}{2} & 0 \\ 0 & 0 & 0 & 0 & 0 & \frac{1-2\nu}{2} \end{bmatrix} \tag{24}$$

Three distinct coatings are subjected to investigation, necessitating the determination of Young's modulus and Poisson ratio for each (as depicted in Table 2). The simulation yields the mode shapes displayed in Figure 32. Through the relative displacement plots, COMSOL® solves the integrals presented in Table 1, enabling the derivation of the energy ratio required to apply Equation 16.

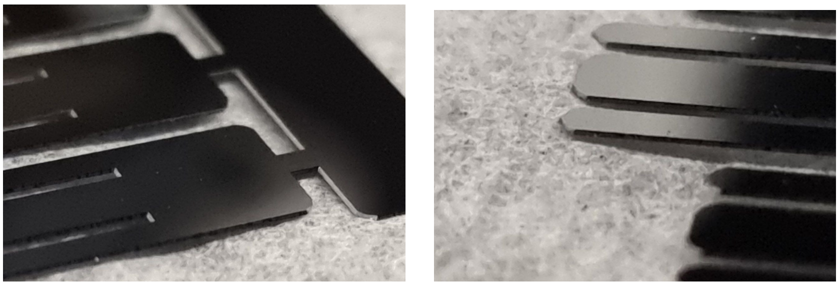

(a) Tridents' point of attachment to the base.

(b) Tridents' "fingertips".

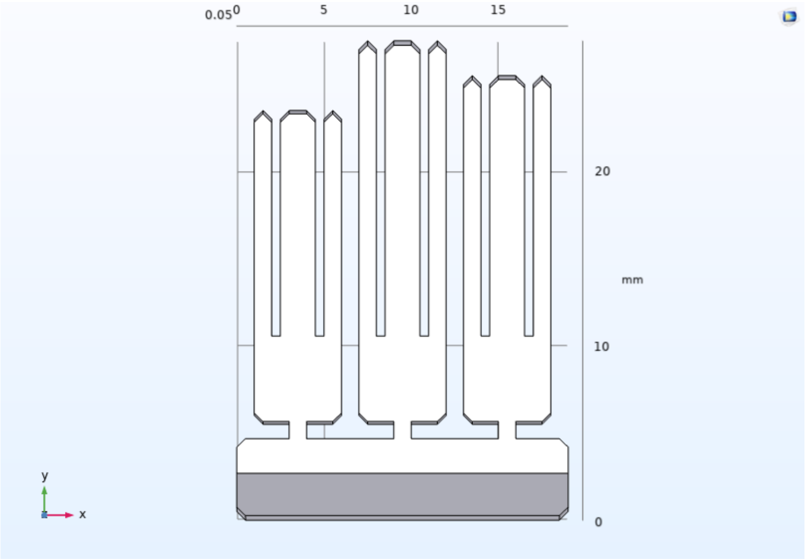

(c) 2D view of the modeled geometry.

Figure 31: Close-up images of uncoated tridents and geometrical model on COMSOL®. The bottom side of the base, separated by the rest with a work-plane, is used as a fixed constraint for the eigenfrequency study, as that section is clamped for both the deposition process and the measurements.

MATERIAL	YOUNG'S MODULUS	POISSON RATIO
1. Amorphous GeO_2	(43 ± 0.8) GPa	0.29 ± 0.04
2. $\mathrm{Ti}:GeO_2$ (44%)	(75 ± 1.3) GPa	0.31 ± 0.03
3. $\mathrm{Ti}:SiO_x$ (66%)	(108 ± 3.0) GPa	0.38 ± 0.1

Table 2: The elastic characteristics of the coatings under investigation were ascertained experimentally by the frequency shift of a 75mm disk's resonant frequencies before and after the coating process [27].

5.3.2 *Microfabrication*

The accurate fabrication of silicon microresonators with complex shapes requires a full photolithographic process to be performed in *clean-*

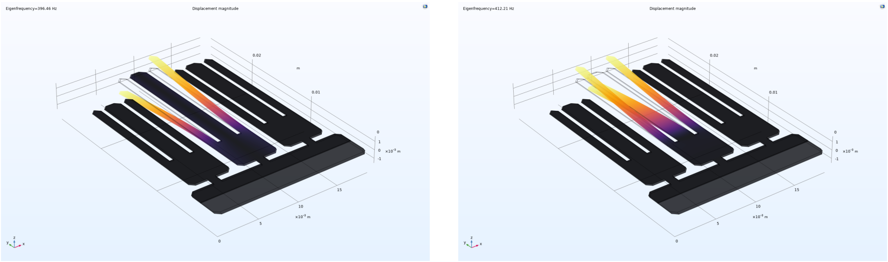

(a) Long AS1 - 396.46 ± 0.2 Hz (b) Long AS2 - 412.21 ± 0.2 Hz

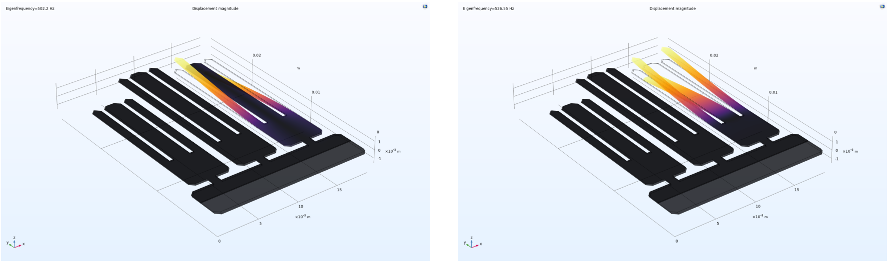

(c) Mid AS1 - 502.2 ± 0.2 Hz (d) Mid AS2 - 526.55 ± 0.2 Hz

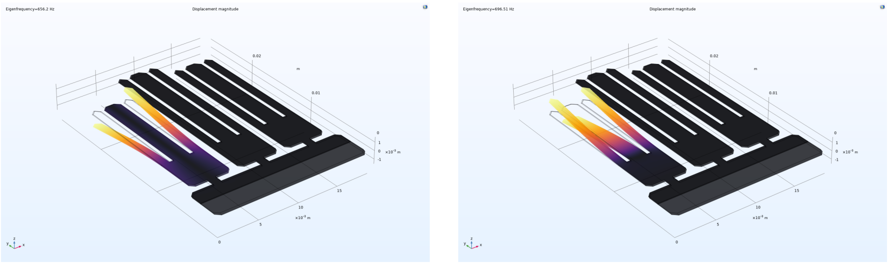

(e) Short AS1 - 656.2 ± 0.2 Hz (f) Short AS2 - 696.51 ± 0.2 Hz

Figure 32: In the trident resonators, 6 high Q-factor modes are identified through Finite Element Method (FEM) analysis in the low-frequency range. The frequencies presented pertain to ideal samples, implying that some deviation can be anticipated when experimentally detecting the resonant peaks. Moreover, the resonant mode frequencies may shift when applying different coating materials, but, given the relative dimension of the monolayers with respect to the substrate, the impact is expected to be negligible and within the error of the simulation.

room, with particular attention to the delicacy of the substrate, being a 100 µm thick (100) Silicon 4-inch wafer. This also means that common rinsing tools such as spin rinse driers are to be avoided. The procedure will be explained step-by-step.

A nanofabrication cleanroom is a controlled environment, maintained at ultra-low levels of contaminants, specifically designed for the precise manufacturing and manipulation of nano-scale structures and devices.

Fabrication Process of Silicon Resonators

1. WAFER CLEANING The silicon wafer is cleaned in Hydrogen Fluoride (HF) to remove any residual oxide on the surface. This step ensures that the surface is adequately prepared for the first depo-

MODE	$Ti:GeO_2$ (44%)	GeO_2	$Ti:SiO_x$ (66%)
longAS1	119.80	202.62	81.63
longAS2	117.18	208.28	83.86
midAS1	120.71	202.84	81.30
midAS2	117.50	210.29	82.68
shortAS1	122.06	203.36	84.62
shortAS2	117.93	206.48	81.72

Table 3: Energy ratios (E_S/E_C) computed using COMSOL®, for all modes of the three materials under investigation. These will allow to compute the coating loss for each material from Equation 16.

sition step, eliminating contaminants that might interfere with the subsequent processes and make this masking layer porous.

2. PLASMA ENHANCED CHEMICAL VAPOR DEPOSITION (PECVD) An 80 nm-thick Silicon Nitride (SiN) layer is deposited on both sides of the Silicon wafer using PECVD. The vacuum chamber is purged with Helium flow, and the substrate is kept at approximately 350°C throughout the process, then left to cool down afterwards.

3. RESIST SPIN-COATING The initial step involves coating the silicon wafer with a resist layer of less than 1 um thickness using a manual spin-coater. The wafer is cleaned using a nitrogen gun if it is fresh; otherwise, a silane oven is employed to remove any residual resist. The wafer is then loaded onto the right chunk of the machine, and the recipe for resist SPR3612 is applied, spinning the wafer at about 5000 rpm. SPR3612 is a well-established i-line positive resist commonly employed in the Stanford Nanofabrication Facility (SNF). After coating, the wafer is pre-baked at 90°C for 1 minute. The mask is then aligned with respect to the wafer's cut, ensuring that the crystalline plane of the wafer is parallel to the resonators' edge line, enhancing the robustness of the etched resonators. The mask is shown in Figure 33.

In this context, i-line *refers to a specific wavelength of near-ultraviolet light, around 365 nanometers, commonly used in photolithographic processes.*

4. ULTRAVIOLET (UV) EXPOSURE The coated wafer undergoes UV exposure using a mask aligning machine. The exposure is performed in soft contact mode (no vacuum between mask and substrate) with a distance of 50 μm between the mask and wafer. The exposure time is set to 5 seconds, allowing the exposed resist's photoactive compound to react and make the film soluble in the developer solution. Fine alignment using the machine tools is not necessary, as with a flexible soft mask one can build a pocket to fit the wafer inside and in the correct position.

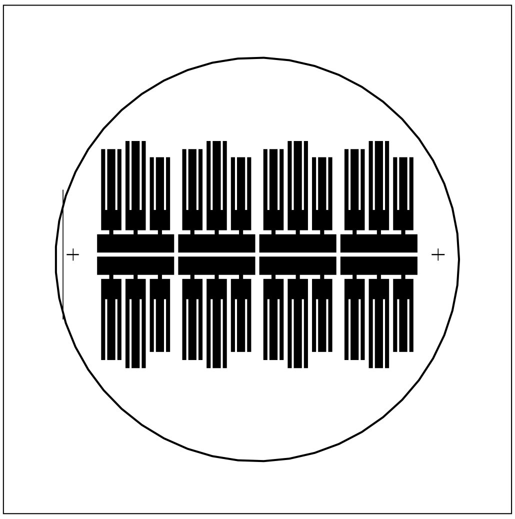

Figure 33: The mask comprises a polyester film coated with a photosensitive emulsion on one side. To facilitate its use, it requires a clear glass mask as a supporting element for insertion into the exposure machine. Notably, a 4-inch wafer accommodates eight triple-trident resonators.

5. POST-BAKE The wafer is post-baked at 115°C for 1 minute. This step helps after exposure to finalize and enhance the chemical reactions within the photoresist. It improves image quality, stabilizes the latent image, hardens the resist, removes residual solvents, and ensures uniformity, avoiding standing-wave patterns on the edges of the resist.

6. DEVELOPMENT The wafer is developed using MF26-A for 30 seconds, with constant stirring to ensure uniform development. It is then rinsed with water at least three times and dried with a nitrogen gun. This step removes the unexposed resist, revealing the underlying material for etching. MF-26A is a commercial developer for i-line resists that contains 2.5% TMAH (Tetramethylammonium hydroxide) and 1% polyglycol in aqueous solution.

SCCM stands for Standard Cubic Centimeters per Minute. The "standard" conditions typically refer to a temperature of 273.15 Kelvin and a pressure of 1 atmosphere. SCCM quantifies the volume of gas, measured in cubic centimeters, that passes through a given point in a system in one minute.

7. DRY ETCHING USING REACTIVE ION ETCHING (RIE) The wafer undergoes dry etching. The process parameters include Oxygen and Freon (CHF3) gas at rates of 15 sccm , RF power of 50V, and a chamber pressure of 50 mTorr. The etching duration is established at 5 minutes, effectively eliminating the 80nm-thick SiN layer in areas where the resist has been dissolved. This process selectively retains the SiN masking layer exclusively on the tridents' structure.

8. WET ETCHING USING KOH The wafer is then subjected to wet etching using a KOH (Potassium Hydroxide) solution. The solution is prepared by mixing 1750 ml of 45% KOH with 750 ml of DI water. The

solution is heated to 90°C, and the wafer is etched for approximately 1.5 hours, depending on the resulting thickness. This step is critical for separating the resonators from the wafer.

9. WET ETCHING USING HYDROGEN FLUORIDE (HF) FOR SIN REMOVAL Finally, the separated resonators undergo wet etching using HF to remove the SiN mask. The resonators are dipped into a 49% HF solution for 2 minutes, followed by rinsing with DI water. The HF etching leaves the silicon resonators with a hydrophobic surface, facilitating drying. The resulting silicon resonators exhibit a shiny mirror surface, indicating successful fabrication.

6

CHARACTERIZATION OF AMORPHOUS COATINGS: RESULTS

The amorphous coatings are fabricated using the Ion Beam Sputtering (IBS) technique. In this process, ions are accelerated and directed towards a target material (typically Germanium, Titanium, or Tantalum), causing sputtering of atoms or molecules from the target, which subsequently condenses on the substrate as a thin film. The sputtered coatings are then subjected to oxidation in an O_2 atmosphere inside the chamber.

However, achieving ideal and uniform oxidation in the thin films is challenging, leading to the formation of defective regions, such as metallic clusters, causing high optical absorption due to trap levels in the film's forbidden bandgap. To address this, post-deposition annealing in air is often performed. This process diffuses oxygen within the film, promoting homogeneity and relieving stress induced during deposition. It is crucial to control the annealing duration as longer times may induce crystallization in the amorphous film, which is undesirable. Crystalline grain boundaries act as scatterers, leading to a degradation of the film's optical quality. The extent of crystallinity will be further investigated in Section 6.3.

The materials being studied were deposited on both the tridents and on 3-inch IR-grade Fused Silica substrates. These Fused Silica substrates were employed for optical absorption and crystallinity measurements.

6.1 MECHANICAL LOSS

6.1.1 *General Remarks*

A. The preliminary step in calculating the mechanical loss of the coating in question involves conducting temperature-dependent mechanical loss assessments of the high Q-factor modes in uncoated tridents. These readings will subsequently offer a reference point for the application of Equation 16. Through this investigative process, several intrinsic properties and inherent limitations of these resonators became evident:
    - The AS2 modes demonstrate increasing difficulty in detection upon cooling towards liquid Helium temperatures, often being obscured by system noise (encompassing both optical and mechanical facets). A similar observation is noted in the Double-Paddle Oscillator (DPO) [22], an es-

tablished resonator integral for mechanical loss measurements, albeit with a singular high-quality mode. To enhance the specific excitation of anti-symmetric modes, the preliminary alteration would entail fine-tuning the actuator. This modification should be engineered to selectively excite a trident in an anti-symmetric manner.

- Paradoxically, even though AS2 modes are challenging to stimulate effectively, they manifest a reduced mechanical loss compared to their AS1 counterparts. This can be attributed to the AS1 modes imposing a marginal torque on the base, leading to a subtle dampening effect due to the clamp. While this serves as an effective validation for the modal nature, it implies that in efforts to delineate a frequency dependency for the material's mechanical loss, the two modes might exhibit distinct behaviors.
- At elevated temperatures (exceeding 200K), thermoelastic loss predominantly governs the mechanical loss. Consequently, results procured in this temperature domain may exhibit non-deterministic tendencies. However, the focal interest of this study gravitates towards the lower temperature spectrum.

Thermoelastic loss emerges when a material experiences vibration or mechanical deformation, inducing stretching and compression of its internal bonds. This deformation instigates interatomic frictions and interactions, precipitating heat generation within the material. The resultant heat translates to a dissipation in the mechanical energy of the vibrating system.

- Upon cooling, there is a noticeable upward shift in the resonant frequencies of all modes, typically in the range of 2-4 Hz. This can be attributed to the tridents' thermal compression, which results in inconsistent mechanical structure of the resonators across all temperatures. While this effect doesn't influence the results significantly, it remains a noteworthy observation.
- Interestingly, the behaviors of the '**longAS1**' and '**shortAS1**' modes often exhibited a unique trend, as depicted in Figure 34. For these specific modes, the initial phase of the ringdown appears to follow a quadratic decay, which subsequently transitions into an exponential decay. A study conducted by O. Shoshani et al. [21] elucidates this phenomenon. In nanomechanical systems, when two resonant modes, having frequencies that are integral multiples of each other, are concurrently excited, a non-linear coupling can manifest. Given that the fundamental modes (where the entire trident oscillates relative to its base) are perpetually in a state of vibration — albeit with notably low Q — and considering that the frequencies of two of these fundamental modes are approximately half of those associated with the aforementioned AS1 modes, it's plausible that this non-linear quadratic effect is being activated, espe-

cially since the current actuator tends to exert electrostatic force on all three tridents at the same time.

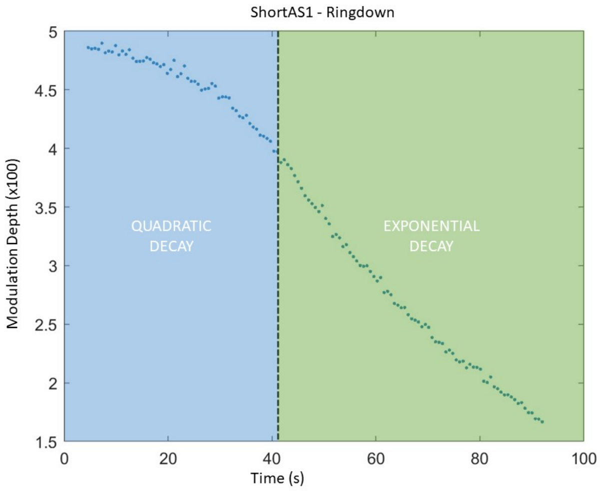

Figure 34: Germania-coated sample shortAS1 ringdown captured at ~80K. The y-axis value shows the y-oscillation AC signal, amplified 100 times and normalized over the measured DC signal.

B. Based on the data procured from the lock-in amplifier, which processes the ′**sum**′ signal from the quadrant photodetector, a discernible trend emerges: the total power incident upon the detector diminishes with decreasing temperature. This phenomenon could be attributed to various factors, including potential degradation in material reflectivity or the activation of absorption/scattering processes in either the material or the cryostat window itself. In the context of reflectivity, an in-depth examination was undertaken on the mirrors used in KAGRA [24]. The findings indicated that, even under optimal vacuum conditions, there is a likelihood of ice formation on the surface of the coating at sub-zero temperatures. However, it's worth noting that these observations were made over extended durations, suggesting that the rate of ice accrual might be too minimal to account for the pronounced change in power observed during rapid cooldowns from ambient temperature to 80K — a transition typically completed within roughly 30 minutes. Conversely, the vacuum quality attainable with the system utilized in this study is 3 to 4 orders of magnitude inferior to that of KAGRA. This discrepancy notably influences the time constant associated with ice formation. The rate of ice formation in vacuum environments has been investigated by E. Bonilla, a member of LIGO, in an internal document [6]. Bonilla's findings indicate that at low temperatures, when the water's partial pressure is akin to the vacuum level attained in the current experimental setup, ice can accrue at a rate of approximately 1 µm per day. This suggests

that, by the culmination of the cooling cycle, the thickness of the ice layer might approach or even surpass that of the coating. The precise ramifications of this thin ice layer on the system's behavior remain to be elucidated; however, its potential influence warrants further exploration.
The root cause of this experimental observation remains elusive and could likely be a composite effect of multiple contributing factors. These may as well encompass ice accretion on the cryostat windows, alterations in the optical properties of materials at diminished temperatures (which warrants a comprehensive investigation), or potential deformations in the resonators. The latter could result in modulated reflected power due to minute alterations in the lasers' incidence angles on the tridents.

c. One pivotal consideration in the experimental setup relates to the impact of laser optical noise. The sensitivity of the setup can be hindered, particularly towards the more subtle modes, due to this noise. To counteract common mode noise and offsets — which could adversely influence the '**sum**' signal, representing the aggregate power received by the detector — several enhancements were made in the experimental code for subsequent measurements. Specifically, the AC signal in the y-direction is now normalized to the DC power. The AC signal, in turn, undergoes amplification by a factor of 100 through the employment of a low-noise pre-amplifier, as depicted in Figure 27. Furthermore, the interface between the DAQ (Data Acquisition) system and LabVIEW witnessed the following enhancements:

   - Invoking the Nyquist theorem, it is established that for accurate signal reproduction, the sampling frequency should exceed twice the maximum frequency inherent to the signal. Given that the uppermost frequency necessitating scrutiny corresponds to the '**shortAS2**' mode — approximately 800 Hz — the sampling rate has been calibrated to 2 kHz, affording a margin for potential discrepancies.
   - The employed code leverages the Fast Fourier Transform (FFT) approach when seeking specific frequencies within the sampled signal. The intricacies of FFT dictate that frequency resolution can be refined by sampling over extended signals, meaning a greater number of cycles. Acknowledging the potential influence of noise, coupled with the unspecified nature of the sampling window function adopted by LabVIEW, a sampling window spanning 1000 samples (with a 1kHz rate) has been empirically validated as efficacious.

6.1.2 *Bare Tridents*

As previously discussed, the initial step in quantifying the mechanical loss of coatings involves measuring the baseline loss of an uncoated substrate. This provides a reference point from which the loss associated with the coated sample can be determined, taking into account the proportional elastic energy retained in both the coating and substrate. While the curves depicting mechanical loss across varying temperatures are anticipated to predominantly reflect the properties of the materials under study, the specifics of the experimental setup can introduce nuances. This is due to the disparate temperature-dependent behaviors exhibited by the materials constituting different components of the setup. These subtle variations could slightly alter measurement conditions. Additionally, the relative amplitude (or measured oscillation intensity) of each mode within a given category (be it AS1 or AS2) may be influenced by the resonator's quality. Given that this quality might display inconsistencies during the manufacturing phase, it is conceivable that those specific modes, which might elude detection due to the sensitivity constraints of the current setup, won't necessarily be consistent across all samples.
The salient findings for the uncoated sample are delineated in Figures 36 and 37. As can be observed in Figure 36b, a minor peak around ~28K is evident. Notably, this peak also manifests in coated samples, albeit with varying magnitudes, that is, different damping strengths. In an antecedent experimental setup, the clamp was constituted of INVAR as opposed to the present Be-Cu configuration. Given the peculiar behavior of INVAR's linear thermal expansion coefficient — exhibiting a negative minimum in the vicinity of the aforementioned temperature (refer to Figure 35) — the difference in thermal compression between the resonator's base and the clamp was conjectured to be the origin of the observed peak in loss. Nevertheless, after transitioning to the Be-Cu clamp, the mysterious peak persists and remains an enigma and, as a consequence, it may be ascribed to some still undiscovered cryogenic properties of Silicon.

6.1.3 *Coated tridents*

Deposition of a different material as a thin layer onto silicon substrates introduces additional sources of non-uniformity and noise that might compromise the precision of the setup. Non-uniform or defective coatings can result in the disappearance of more modes across various temperature ranges. Furthermore, applying the coating solely on one side of the substrate poses another challenge: the disparity in thermal expansion coefficients between the substrate and the coating induces stress mismatches, leading the resonator to deform with temperature fluctuations. This effect, amplified at elevated

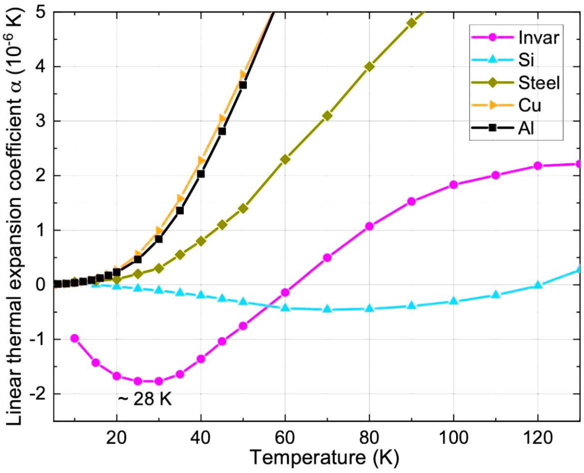

Figure 35: Linear Thermal Expansion Coefficient for several pertinent materials, computed using the NIST material properties calculator [23], and subsequently visualized.

temperatures, is particularly pronounced during nitrogen measurements. Depending on the specific sample, maintaining the alignment of the laser beams onto the photodetector can become increasingly arduous due to this deformation. However, as hypothesized, coating both sides of the sample effectively mitigated this issue. The residual minor deformation, which remains manageable, likely arises from a stress mismatch with the clamp. This phenomenon was substantiated when mechanical loss measurements, initiated at a chilled 12K and extended up to 80K, exhibited heightened mechanical loss during the temperature ascent. This suggests that the descending temperatures inadvertently weakened the clamping grip, as depicted in Figure 38. To rectify this, the clamp's elasticity was enhanced by integrating soft indium wire, which retains its pliability even at cryogenic temperatures, beneath the clamp's screw.

Mechanical loss measurements for each coated sample were conducted both pre and post-annealing at 600°C for a duration of 10 hours. Subsequent Figures 39 and 40 will depict key results, elucidating the coating quality and the setup's proficiency.

To derive the coating loss from the data captured on both bare and coated tridents, we considered data points obtained at specific temperatures (within a tolerance of ±2K). The equation employed for this purpose is Equation 16. The sensitivity of our experimental setup was adequate to successfully subtract the mechanical loss of the uncoated sample from that of the coated sample, especially in the lower temperature range. This subtraction was carried out after scaling by the energy ratios as delineated in Table 3. Notably, certain anomalies were observed for temperatures exceeding 200K, potentially attributable to the impact of thermoelastic loss in that temperature bracket. Repre-

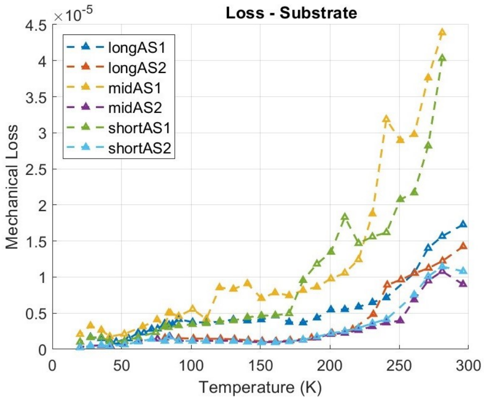

(a) Mechanical Loss curves for all modes of the bare resonator. As anticipated for Silicon, the mechanical loss typically diminishes with decreasing temperature. Beyond 200K, the pattern, as predicted, becomes more erratic due to thermoleastic contributions.

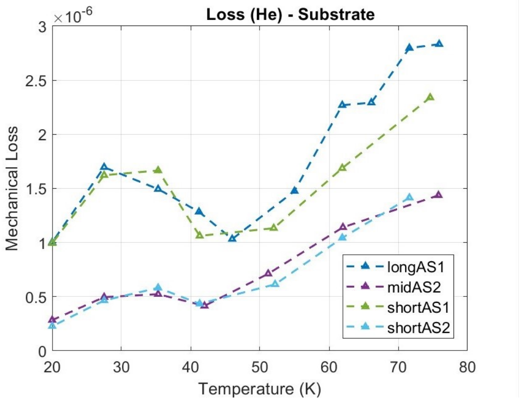

(b) A magnified representation for temperatures below 80K, necessitating liquid Helium for sample cooling. All enduring modes exhibit a peak at ~28K, in agreement with observations from the DPO resonator, the genesis of which remains unresolved.

Figure 36: Mechanical loss characteristics of the uncoated resonator at various temperature scales.

sentative plots of these observations can be discerned in Figures 41 and 42.

6.2 OPTICAL ABSORPTION

The PCI setup, described in depth in Chapter 3, extensively relies on the Fused Silica substrate for its operation. A probe with a distinct wavelength is employed to measure amorphous coatings, precisely 632 nm. This selection is justified when we compare amorphous coatings with their AlGaAs-based counterparts. The latter kind absorbs

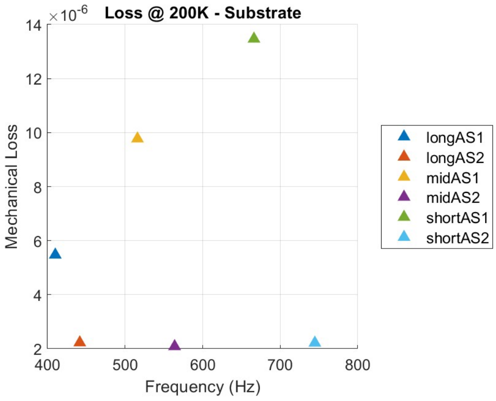

(a) A presentation of the Mechanical Loss across all six modes of the bare tridents at 200K. This aims to elucidate the frequency-dependent behavior of this loss. As alluded to earlier, the AS2 modes generally manifest a reduced loss compared to the AS1 variants, though they operate within a comparable magnitude.

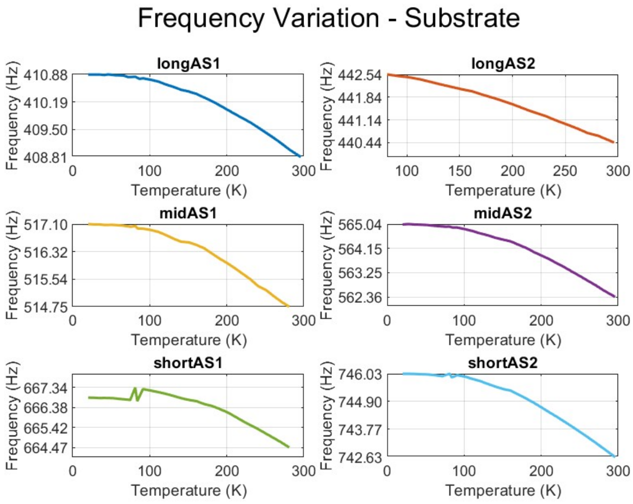

(b) The resonance frequencies of all modes decrease with temperature, sharing a congruent dependency.

Figure 37: Resonant mode's frequency temperature-dependent analysis for bare tridents.

in the visible spectrum, while the former does not. Given this non-absorptive nature in the visible range, the use of a visible laser probe becomes not just apt but also significantly convenient, especially during the alignment phase. Therefore, it is the preferred choice for this setup. The PCI measurements detailed in this section necessitate the determination of absolute optical absorption values, which is achieved by integrating Equation 11 into the LabVIEW code. Post-annealing, there's an anticipation of reduced optical absorption values, indicative of a more uniform sample. However, this expectation

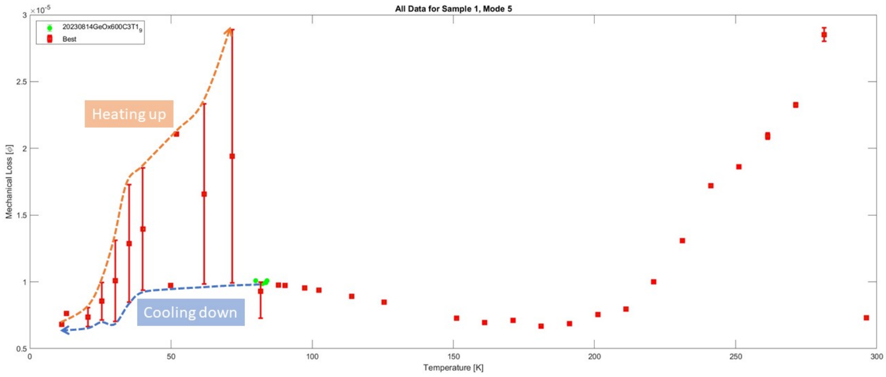

Figure 38: Prominent divergence in mechanical loss was observed between the cooling and subsequent heating phases. Distinct measurement runs are demarcated by the colored arrows.

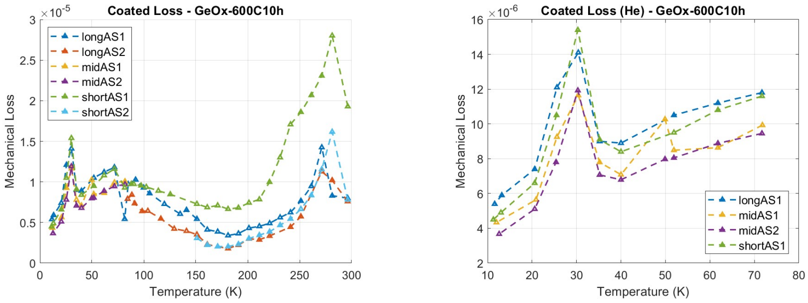

(a) Mechanical loss curves for the coated sample. Above 200K, the behavior is similar to the bare tridents. However, a discernible increase in loss is evident as temperature decreases, which aligns with expectations for amorphous coatings. At lower temperatures, the loss values considerably exceed those observed for bare tridents. This pronounced difference facilitates the computation of the coating loss, given the setup's sufficient sensitivity to discern between the losses.

(b) The peak around ~ 28K is more pronounced in the coated sample compared to the bare tridents. Typically, 2 of the AS2 modes are masked by the system noise at extremely low temperatures.

Figure 39: Mechanical loss for the Germania-coated sample post-annealing.

was not met for every sample examined, leading to an inference that the coating quality of certain samples might have been subpar. A perfect example is shown in Figure 43. To evaluate the optical absorption of a designated sample, the subsequent procedure is executed:

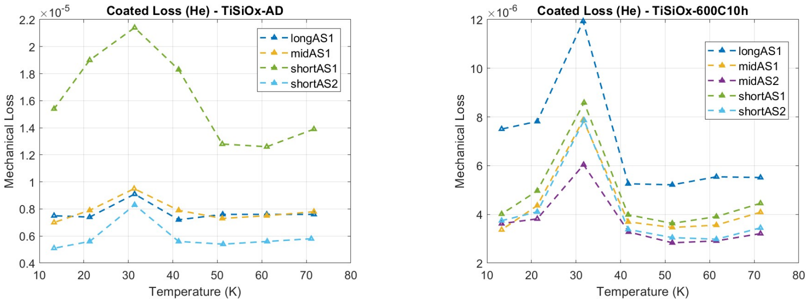

(a) Pre-annealing, the peak around ∼ 28K appears more attenuated. Ideally, the **'shortAS1'** mode values should align closely with those of the other AS1 modes; the observed disparity is likely attributable to the coating's non-uniform distribution across the tridents.

(b) Post-annealing, the peak exhibits a steeper incline across all modes. The **'shortAS1'** mode, which previously displayed higher loss, seems to have converged to more standard values. Interestingly, the **'midAS2'** mode was discernible within the Helium range, showcasing the lowest values. This observation aligns with the notion that modes that are more challenging to excite often correspond to lower mechanical loss values.

Figure 40: Mechanical loss of $\mathrm{Ti}:\mathrm{SiO_x}$-coated samples in the Helium range, pre and post-annealing.

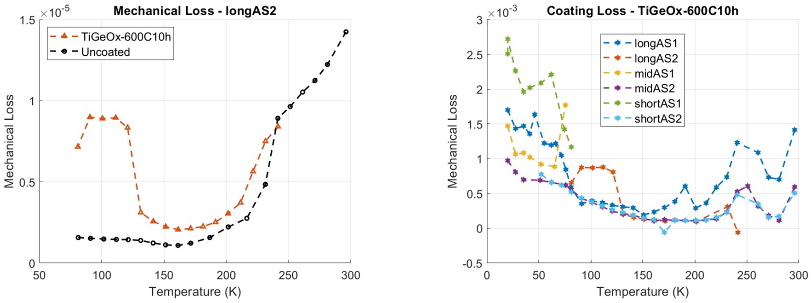

(a) By juxtaposing the curve of the uncoated sample with that of the coated, the pronounced contribution of the coating to the overall sample loss becomes evident. There's a marked rise in coating loss upon cooling.

(b) Subsequent to the calculations, the deduced coating loss is of the order of 10^{-3}, aligning with previous readings obtained using DPOs. The higher temperature range, however, presented less predictable trends, including some data points registering negative values. This negative anomaly arises when the uncoated resonator exhibits a lower quality factor than its coated counterpart.

Figure 41: Mechanical loss observed in $\mathrm{Ti}:\mathrm{GeO_2}$-coated samples after the annealing process.

1. At a predefined point on the sample, a z-scan is carried out to illustrate the interference pattern and to determine the central peak absorption value. If this absorption value is exceedingly

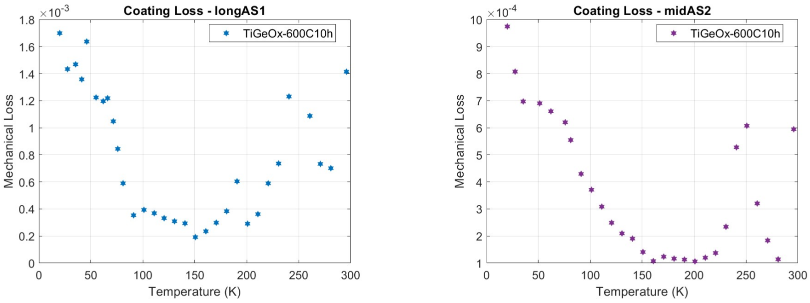

(a) (b)

Figure 42: Mechanical loss values for the $\mathrm{Ti}:\mathrm{GeO}_2$ coating for two distinct mode shapes. Even post-coating contribution extraction, the AS2 mode exhibits a lower loss.

low, the background of the substrate should be deducted. This can be achieved by extending the z-scan (as demonstrated by Figure 11) until the substrate is reached and then subtracting half of the acquired substrate absorption value. This rationale is grounded in the fact that the sample, constructed of a thin layer on the Fused Silica (FS) substrate surface, transitions its substrate PCI signal from the inherent substrate value to the air medium value (which is practically negligible) when at the surface. This is essentially a median value at the interface of these two media, namely, the surface.

2. This step involves repeating the aforementioned operation at a new point, positioned 10 millimeters from the original in the x-direction. It's imperative to ascertain the depth where the absorption peak manifests. Should this depth deviate from the one observed at the original point, a compensatory adjustment is implemented in the program for the subsequent scan.

3. Commencing from the initial point and concluding at the second, and centering the pump-probe intersection at the focal plane identified with the z-scan, a 10 mm x-scan is undertaken. Throughout this procedure, the data plot is subjected to filtering by averaging multiple results for each discrete point. This endeavor aids in highlighting the baseline absorption of the sample and may additionally highlight potential aberrations or imperfections along the examined trajectory.

Following the investigation of the initial batch of samples, a subsequent 3-inch FS substrate was coated with a layer of $\mathrm{Ti}:\mathrm{GeO}_2$ measuring 250 nm in thickness. This was done in order to align with the new tridents assessed in the mechanical loss setup. A comprehensive discussion about the obtained results can be found in Figure 44. It's imperative to deduct approximately 0.6 ppm from the nominal value, taking into account that the bulk absorption value, as depicted in Figure 11, stands at 1.2 ppm. A tabular summary of results for all analyzed samples is presented in Table 4. Notably, the GeO_2 sample, prior to annealing, displayed an exceptionally low baseline absorption. However, the plot unveiled numerous defective regions, possibly elucidating the post-annealing surge in absorption.

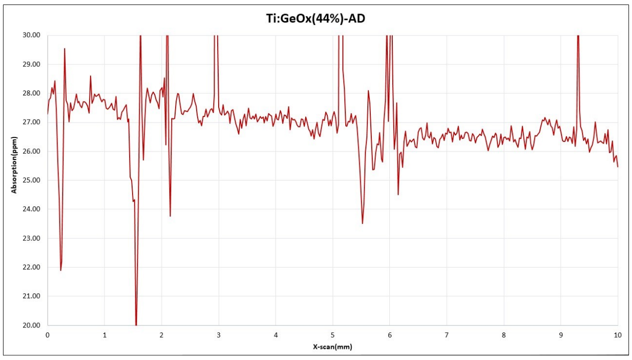

(a) PCI x-scan of a 500 nm AD $\mathrm{Ti} : \mathrm{GeO}_x(44\%)$ sample. Throughout the scan, there's a slight decline in baseline optical absorption from 27.5 ppm to 26.5 ppm. This indicates a possible drift in the AD coating, potentially originating from the deposition process. Subsequent z-scans at both ends confirmed a consistent depth for the interference peak, effectively eliminating misalignment as a potential cause.

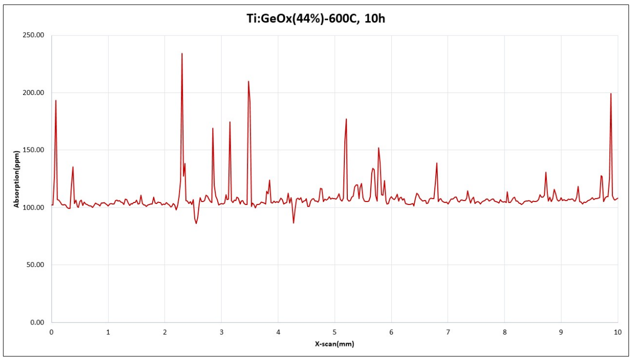

(b) PCI x-scan of 500 nm $\mathrm{Ti} : \mathrm{GeO}_x(44\%)$ after undergoing 10 hours of annealing at 600°C . The 105 ppm baseline renders it unsuitable for LIGO standards. Such an observation is unanticipated and hence, is more likely attributed to an unidentified deposition issue inherent to the entire coating.

Figure 43: Comparative PCI x-scans for $\mathrm{Ti} : \mathrm{GeO}_x(44\%)$ coatings of 500 nm thickness, detailing both pre and post-annealing states.

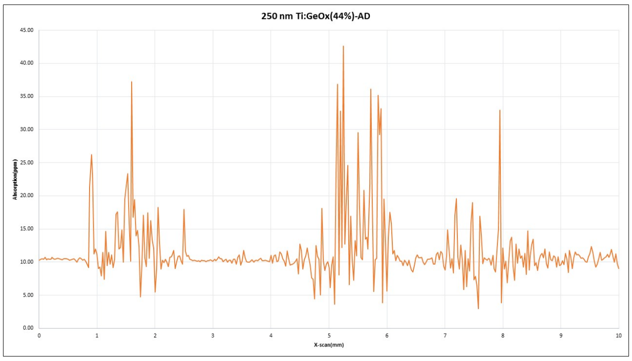

(a) PCI x-scan of a 250 nm AD $\mathrm{Ti : GeO_x}$ (44%) coating. The baseline optical absorption remains stable at 10.8 ppm throughout the scan, yet notable defects are discernible, with absorption peaks reaching up to 40 ppm.

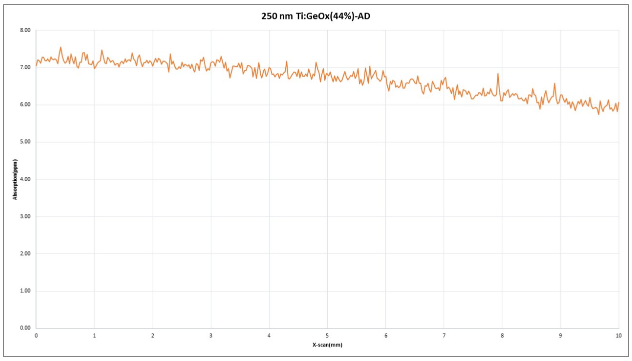

(b) PCI x-scan of 250 nm $\mathrm{Ti : GeO_x}$ (44%) after 10 hours of annealing at 600°C . The baseline displays a descending trend from 7.25 ppm to 6 ppm. The post-annealed sample exhibits improved uniformity with an absence of defects. The annealing process in this context successfully enhanced optical absorption characteristics.

Figure 44: Comparative PCI x-scans for $\mathrm{Ti : GeO_x}$ (44%) coatings of 250 nm thickness, elucidating both pre and post-annealing scenarios.

	$\mathrm{Ti : GeO_2}$	$\mathrm{GeO_2}$	$\mathrm{Ti : SiO_x}$
AD (500 nm)	27 ppm	1.2 ppm	24 ppm
600°C , 10h (500nm)	105 ppm	13 ppm	14 ppm
AD (250 nm)	10 ppm	-	-
600°C , 10h (250 nm)	6 ppm	-	-

Table 4: Tabulated summary of PCI-measured absorption values for the range of coatings studied. It has been established that optical absorption increases nearly linearly with coating thickness. Thus, for a preliminary comparison between the 250 nm coating values and prior measurements, one can approximately double the values as a first-order estimation.

6.3 CRYSTALLINITY

6.3.1 *Employing XRD for the Characterization of Amorphous Coatings*

X-ray diffraction (XRD) is premised on the interaction between X-rays — electromagnetic waves with wavelengths of the order of atomic dimensions — and matter. When high-energy electrons are directed onto an anode material, such as Copper, they displace the inner shell electrons of the target atoms. $K\alpha$ is the characteristic X-ray emission line that indicates the transition of an electron within the Cu atom's innermost shell, and it's one of the most commonly used radiations for XRD characterization.

Copper's $K\alpha$ X-ray radiation possesses a high intensity and suitable wavelength (1.54056 Angstroms) for probing crystal lattice spacings. This emission line's moderate penetration depth accommodates varying sample thicknesses, while its narrow linewidth contributes to enhanced diffraction pattern resolution. Moreover, copper is an accessible and cost-effective source.

In XRD, this specific X-ray wavelength is directed at a crystal sample. The resulting diffraction pattern helps determine the arrangement of atoms within the crystal lattice, providing insights into its structure. The choice of X-ray source, like using copper's $K\alpha$ line, impacts the sensitivity obtainable for different diffraction angles, hence each anode is suited for a certain class of materials. Different sources are used based on the sample's properties and the desired information. As electrons from higher energy levels transition to fill these vacancies, they emit X-rays with wavelengths characteristic of the specific electronic transitions. These are known as the characteristic X-rays. Apart from these characteristic peaks, the bremsstrahlung (or *braking radiation*) process, wherein accelerated electrons are decelerated upon interaction with atomic nuclei, produces a continuous X-ray spectrum, contributing to the background in XRD patterns.

The Bragg-Brentano configuration, a cornerstone in XRD studies, operates on the principle that crystalline materials will diffract X-rays at specific angles. This is based on Bragg's law, which relates the angle of incidence, the wavelength of X-rays, and the spacing between atomic layers. When the angle of incidence conforms to this law, a peak is detected, signifying the presence of a specific crystalline plane.

For the study of polycrystalline or amorphous materials, on the other hand, this approach holds limitations. In the *grazing angle* technique, the X-ray beam, rather than being pinpointed, is cast diffusely across the surface. This approach ensures that regions of varying crystallinity or amorphous nature across the sample are all probed, providing a more holistic view of the material's structure. Particularly, if a material exhibits sporadic crystalline regions amidst a largely amorphous matrix, the Bragg-Brentano method may not accurately capture the complete structural heterogeneity.

Due to their lack of long-range periodic order, amorphous materials produce diffraction patterns that starkly contrast with their crystalline counterparts. Rather than distinct, sharp peaks, the patterns reveal a broadened hump. This is often centered around where one would expect the primary peak for a similar crystalline material, and it is indicative of the material's short-range order. While the atoms in amorphous materials are not arranged in a repeating, long-range pattern, they are not in complete disarray either. The broad peak observed in XRD plots indicates the average distance between neighboring atomic or molecular entities — the first coordination sphere. This information, though not as definitive as the detailed peaks from crystalline samples, provides valuable insights into the average local environment within the amorphous material.

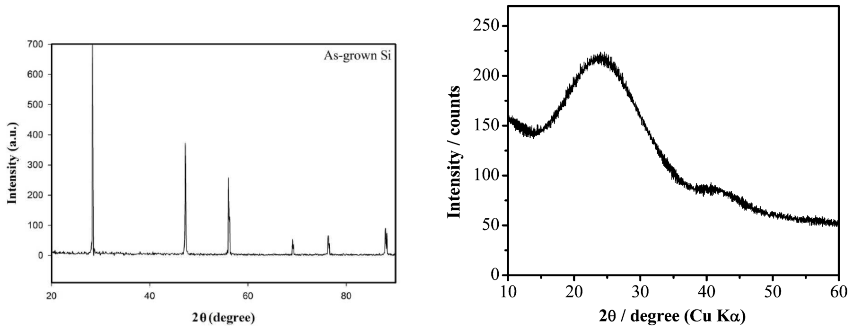

(a) XRD pattern in Bragg-Brentano configuration for crystalline Silicon [3]. If the sample is high-quality, the peaks should be characterized by a narrow FWHM, reflecting minimal instrumental broadening.

(b) XRD pattern for amorphous carbon [4], typical of a uniformly amorphous material. This shape serves as a benchmark for the oxides discussed in subsequent sections.

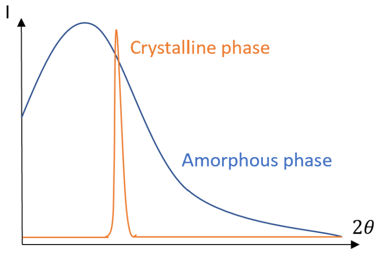

(c) The composite XRD profile for a semi-crystalline sample emerges from the convolution of the amorphous phase with the crystalline phases. To determine the average grain size, one should evaluate the peak width after subtracting the amorphous background, which is typically accomplished using laboratory software.

Figure 45: XRD patterns highlighting the difference between crystalline and amorphous materials.

One of the key applications of XRD is the determination of crystallite size in polycrystalline samples. The Debye-Scherrer formula, given by

$$D = \frac{K\lambda}{\beta\cos(\theta)}, \tag{25}$$

where D is the crystallite size, λ is the X-ray wavelength, β is the full width at half maximum (FWHM) of the diffraction peak, and θ is the Bragg angle, provides a direct method to estimate this size (K is called *shape factor* and it is normally assumed to be close to unity). The observed β in an XRD pattern is influenced by both the intrinsic properties of the sample and the instrumental setup. To ensure accurate size determination, it's essential to account for instrumental broadening. This is achieved by measuring the FWHM ($\beta_{\text{instrument}}$) using a standard sample with a well-defined and larger crystallite size. The real broadening due to crystallite size and strain in the sample of interest is then obtained by correcting the observed width: $\beta^2_{\text{corrected}} = \beta^2_{\text{sample}} - \beta^2_{\text{instrument}}$. In the research infrastructure employed for this study, the instrumental broadening was quantified at 0.078 degrees, rendering it essentially negligible.

6.3.2 *Plots*

All samples were analyzed both before and after a 10-hour annealing at 600°C . As mentioned at the outset of this chapter, annealing plays a crucial role in ensuring the homogeneity of the amorphous coating, which in turn enhances its optical quality. However, there's a catch: it could induce unwanted crystallization. A 10-hour annealing might seem inconsequential and, for the finest films, no crystallization is anticipated. This holds for the Germania-based coatings, with no signs of crystallization post-annealing, exemplified by $\mathrm{Ti:GeO_2}$ in Figure 46. Contrarily, $\mathrm{Ti:SiO_x}$ starts revealing early crystallization signs, as depicted in Figure 47. Perfecting the annealing recipe to align with LIGO's stipulations remains a work in progress. Given that a majority of tests involve 100-hour annealing, this outcome might be pivotal in excluding this specific composition for the upcoming mirror iterations.

Anatase is one of the three mineral forms of titanium dioxide. It belongs to the tetragonal crystal system and coexists with rutile and brookite.

6.4 PROPOSED ENHANCEMENTS TO THE MECHANICAL LOSS SETUP

The present mechanical loss setup, delineated in Chapter 5, along with supplementary advancements discussed in Subsection 6.1.1, has commendably facilitated the acquisition of reliable coating mechanical loss measurements, mapped against varying temperatures and frequencies. This accomplishment aligns with the initially set objec-

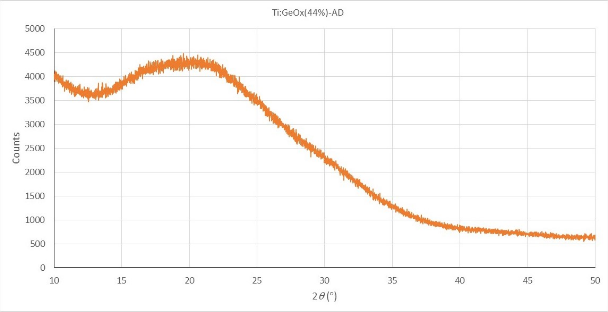

(a) XRD pattern of $\mathrm{Ti}:\mathrm{GeO_x}(44\%)$ as deposited. There's no crystallization trace.

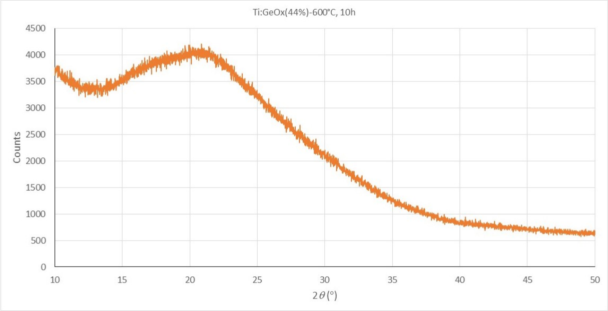

(b) XRD pattern of $\mathrm{Ti}:\mathrm{GeO_x}(44\%)$ post 10 hours of 600°C annealing. The pattern remains largely the same, save for a minor surge in the primary peak, which relates to the first coordination sphere.

Figure 46

tives. However, to further augment the precision, sensitivity, and repeatability across all modes, several refinements can be proposed:

1. **Refinement of the PCB Actuator:** The actuator responsible for trident excitation can be re-engineered with an emphasis on more efficiently resonating antisymmetric modes. This could be achieved by selectively stimulating a single lateral finger for each trident. A more compact and intricate actuator design would also potentially curtail fringe capacitance that arises when all three actuators operate concurrently, by selectively charging the capacitor behind the specific trident of interest.

2. **Enhanced Clamping Mechanism:** Another crucial modification should be the enhancement of the clamping mechanism to minimize variability introduced by human intervention on the clamping force applied to the tridents. Utilizing three distinct, smaller screws - one dedicated to each trident - can ensure a more uniform distribution of the clamping force across the resonators. Specialized Be-Cu washers, supplanting the current indium wire, may bolster the desired spring effect on the clamping screw, thereby improving the overall reliability of the mechanism.

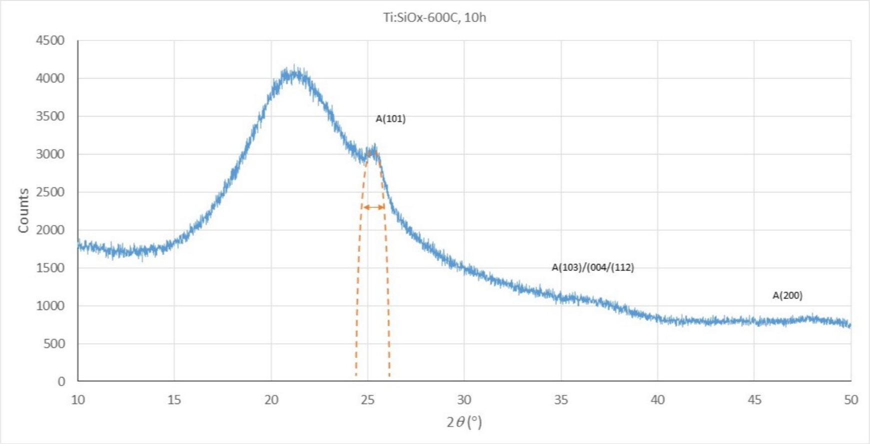

Figure 47: Post-annealing, the $\mathrm{TiSiO_x}$(66%) sample exhibits a pronounced secondary peak, convoluted with the amorphous phase's background, pointing to the <101> crystalline plane of the Titania anatase phase. While this experiment doesn't permit the exact calculation of the ratio between the two phases, as the requisite metric is the area beneath the curves of both phases, the visible peak's width over the background provides an avenue to gauge the mean grain size, using Equation 25, which is calculated to be $D = 11.6$ nm.

3. **Addressing Tension from the Transfer Tube:** Observations during alignment have revealed minor tensions exerted by the transfer tube on the cryostat. Such tensions could influence the system's performance, particularly when flow rates are augmented to achieve lower temperatures. Transitioning to a closed-cycle Helium cryostat offers a solution to this challenge. Notably, a unit has already been procured by the research group.

BIBLIOGRAPHY

[1] J Aasi et al. "Advanced LIGO." In: *Classical and Quantum Gravity* 32 (Apr. 2015). DOI: 10.1088/0264-9381/32/7/074001.

[2] Alexei Alexandrovski, Martin Fejer, A. Markosian, and Roger Route. "Photothermal common-path interferometry (PCI): new developments." In: *Proceedings of SPIE - The International Society for Optical Engineering* 7193 (Feb. 2009). DOI: 10.1117/12.814813.

[3] Khuram Ali, Sohail Khan, Mohd Zubir, and Mohd Zubir Mat Jafri. "Spin-on doping (SOD) and diffusion temperature effect on re-combinations/ideality factor for solar cell applications." In: *Chalcogenide Letters* 9 (Nov. 2012), pp. 457–463.

[4] Sundar Rajan Aravamuthan, Sampath Srinivasan, and Ashok Shukla. "An in Situ Graphite-Grafted Alkaline Iron Electrode for Iron-Based Accumulators." In: vol. 7. Oct. 2013. DOI: 10.1039/c3ee42783h.

[5] Riccardo Bassiri. "The atomic structure and properties of mirror coatings for use in gravitational wave detectors." PhD thesis. University of Glasgow, 2011.

[6] Edgard Bonilla. "Ice layer formation in vacuum environments." In: *Internal Technical Document T1900786, LIGO* (2019).

[7] Herbert B Callen and Theodore A Welton. "Irreversibility and generalized noise." In: *Physical Review* 83.1 (1951), p. 34.

[8] Ondrej Cernotik, Claudiu Genes, and Aurelien Dantan. "Interference effects in hybrid cavity optomechanics." In: (Sept. 2018).

[9] Garrett D. Cole, Simon Gröblacher, Katharina Gugler, Sylvain Gigan, and Markus Aspelmeyer. "Monocrystalline AlxGa1xAs heterostructures for high-reflectivity high-Q micromechanical resonators in the megahertz regime." In: *Applied Physics Letters* 92.26 (July 2008). 261108. ISSN: 0003-6951. DOI: 10.1063/1.2952512. eprint: https://pubs.aip.org/aip/apl/article-pdf/doi/10.1063/1.2952512/13853467/261108_1_online.pdf. URL: https://doi.org/10.1063/1.2952512.

[10] Garrett D. Cole et al. "High-performance near- and mid-infrared crystalline coatings." In: *Optica* 3.6 (2016), pp. 647–656. DOI: 10.1364/OPTICA.3.000647. URL: https://opg.optica.org/optica/abstract.cfm?URI=optica-3-6-647.

[11] DRM Crooks, P Sneddon, G Cagnoli, J Hough, S Rowan, MM Fejer, E Gustafson, R Route, N Nakagawa, D Coyne, et al. “Excess mechanical loss associated with dielectric mirror coatings on test masses in interferometric gravitational wave detectors.” In: *Classical and Quantum Gravity* 19.5 (2002), p. 883.

[12] M. M. Fejer, S. Rowan, G. Cagnoli, D. R. M. Crooks, A. Gretarsson, G. M. Harry, J. Hough, S. D. Penn, P. H. Sneddon, and S. P. Vyatchanin. “Thermoelastic dissipation in inhomogeneous media: loss measurements and displacement noise in coated test masses for interferometric gravitational wave detectors.” In: *Phys. Rev. D* 70 (8 2004), p. 082003. DOI: `10.1103/PhysRevD.70.082003`. URL: `https://link.aps.org/doi/10.1103/PhysRevD.70.082003`.

[13] Jonathan R. Gair, Michele Vallisneri, Shane L. Larson, and John G. Baker. “Testing General Relativity with Low-Frequency, Space-Based Gravitational-Wave Detectors.” In: *Living Reviews in Relativity* 16.1 (2013), p. 7. ISSN: 1433-8351. DOI: `10.12942/lrr-2013-7`. URL: `https://doi.org/10.12942/lrr-2013-7`.

[14] James Hough, BJ Meers, Gavin Newton, Norna Robertson, Henry Ward, G Leuchs, TM Niebauer, A Rudiger, R Schilling, L Schnupp, et al. “Proposal for a joint German-British interferometric gravitational wave detector.” In: (1989).

[15] Jun Jiang, Alec S Mishkin, Kiran Prasai, Rui Zhang, Maher Yazback, Riccardo Bassiri, Martin M Fejer, and Hai-Ping Cheng. “Analysis of two-level systems and mechanical loss in amorphous ZrO2-doped Ta2O5 by non-cage-breaking and cage-breaking transitions.” In: *The Journal of Chemical Physics* 154.17 (2021).

[16] Fabrice Matichard et al. “Seismic isolation of Advanced LIGO: Review of strategy, instrumentation and performance.” In: *Classical and Quantum Gravity* 32 (Sept. 2015). DOI: `10.1088/0264-9381/32/18/185003`.

[17] *Measurements with a Michelson Interferometer*. URL: `https://fizipedia.bme.hu/index.php/Measurements_with_a_Michelson_Interferometer`.

[18] J. G. Rollins, E. Hall, C. Wipf, L. McCuller, K. Kuns, and R. Adhikari et al. *Gravitational wave interferometer noise calculator*. URL: `https://git.ligo.org/gwinc/pygwinc`.

[19] Proceedings SPIE. “Front Matter: Volume 9822.” In: July 2016, p. 982201. DOI: `10.1117/12.2244400`.

[20] Peter R Saulson. *Fundamentals of interferometric gravitational wave detectors*. World Scientific, 1994.

[21] O. Shoshani, S. W. Shaw, and M. I. Dykman. “Anomalous dissipation of nanomechanical modes going through nonlinear resonance.” In: (2017). arXiv: `1702.00769 [cond-mat.mes-hall]`.

[22] Christoph L. Spiel, R. O. Pohl, and Alan T. Zehnder. "Normal modes of a Si(100) double-paddle oscillator." In: *Review of Scientific Instruments* 72.2 (Feb. 2001), pp. 1482–1491. ISSN: 0034-6748. DOI: `10.1063/1.1340559`. eprint: `https://pubs.aip.org/aip/rsi/article-pdf/72/2/1482/10958366/1482\_1\_online.pdf`. URL: `https://doi.org/10.1063/1.1340559`.

[23] National Institute of Standards and Technology. *Cryogenic Material Properties Calculator*. URL: `https://trc.nist.gov/cryogenics/calculators/propcalc.html`.

[24] Jessica Steinlechner and Iain W. Martin. "Thermal noise from icy mirrors in gravitational wave detectors." In: *Phys. Rev. Res.* 1 (1 2019), p. 013008. DOI: `10.1103/PhysRevResearch.1.013008`. URL: `https://link.aps.org/doi/10.1103/PhysRevResearch.1.013008`.

[25] Kip Thorne and Carolee Winstein. "Human Gravity-Gradient Noise in Interferometric Gravitational-Wave Detectors." In: *Physical Review D* 60 (Oct. 1998). DOI: `10.1103/PhysRevD.60.082001`.

[26] Gabriele Vajente et al. "Low Mechanical Loss Coatings for Reduced Thermal Noise in Gravitational Wave Interferometers." In: *Physical Review Letters* 127.7 (2021). DOI: `10.1103/physrevlett.127.071101`. URL: `https://doi.org/10.1103%2Fphysrevlett.127.071101`.

[27] Gabriele Vajente et al. "Low mechanical loss TiO_2:GeO_2 coatings for reduced thermal noise in Gravitational Wave Interferometers." In: (Aug. 2021).

[28] *Vibration Isolation - LIGO Caltech*. URL: `https://www.ligo.caltech.edu/page/vibration-isolation`.

[29] Lin Zhang, Raymond Barrett, Peter Cloetens, Carsten Detlefs, and Manuel Sánchez del Río. "Anisotropic elasticity of silicon and its application to the modelling of X-ray optics." In: *Journal of synchrotron radiation* 21 (May 2014), pp. 507–17. DOI: `10.1107/S1600577514004962`.

[30] B. P. Abbott et al. "Observation of Gravitational Waves from a Binary Black Hole Merger." In: *Phys. Rev. Lett.* 116 (6 2016), p. 061102. DOI: `10.1103/PhysRevLett.116.061102`. URL: `https://link.aps.org/doi/10.1103/PhysRevLett.116.061102`.

[31] B. P. Abbott et al. "Multi-messenger Observations of a Binary Neutron Star Merger." In: *The Astrophysical Journal Letters* 848 (2 2017), p. L12. DOI: `10.3847/2041-8213/aa91c9`.